University of Alberta

Imaging bone fractures using ultrasonic scattered wavefields: numerical and *in-vitro* studies

by

Hongjiang Li

A thesis submitted to the Faculty of Graduate Studies and Research
in partial fulfillment of the requirements for the degree of

Master of Science

Department of Physics

Fall 2011
Edmonton, Alberta

Abstract

Ultrasound has been widely used in medical diagnostic imaging to image soft tissues. Compared with other methods, ultrasound is superior with no ionizing-radiation, easy portability, low cost, and the capability to provide elasticity information. Conventional ultrasound images provide distorted image information when the ultrasound beam is not normal to the bone structures. In this thesis, we present two imaging algorithms: reverse time migration (RTM) and split-step Fourier migration (SSFM), to image long bones using ultrasound. The methods are tested using simulated data sets. The reconstructed images show accurate cortical thickness measurement and provide the correct fracture dip. The images also clearly illustrate the healing process of a 1-mm wide crack with different in-filled tissue velocities simulating fracture healing. Two *in-vitro* examples using fractured bones are also presented. The study has showed that the migration methods have great potential to quantify bone fractures and monitor the fracture healing process.

Acknowledgements

First, I would like to express my thanks to my supervisors, Dr. Lawrence Le, and Dr. Mauricio Sacchi, for offering me the opportunity to learn here in Physics department. With their help, I found the beauties in the inverse problems and started my research in the application of migration to medical ultrasound imaging area. I have benefited a lot from the talks with them. Their patience, enthusiasm and expertise have given me a lot of support and guidance during the research. Also, special thanks to them for their total support when I changed my program from PhD to MSc. I want to thank my teachers giving courses on signal and image processing, Dr. Jeff Gu, and Dr. Roger Zemp, who have brought me to the interesting world of signal and image processing. I have also benefited a lot from many people during my studies. Special thanks to Dr. Edmond Lou, Rui Zheng, Wei Chen in our group and Amsalu Anagaw and Sam Kaplan in Signal Analysis and Imaging Group. In addition, I would also like to thank all the committee members for taking time to review my thesis. I thank all the graduate staff in physics department and other friendly people here in Canada. Finally and importantly, I thank my family and friends for their continuous support and encouragement.

Table of Contents

List of Figures

Chapter 1. Introduction

1.1 Background

It was estimated that more than 2 million fractures occurred in the United States in 2005. This figure is projected to increase by 50% by 2025 (Burge *et al.*, 2007). Fracture accounts for about 24% of injury-related cost, with billions of dollar loss in the United States (Finkelstein *et al.*, 2006). Therefore, fracture diagnosis and care are a major health priority. Although conventional radiography is still the most common means to assess fracture healing, ultrasound assessment is emerging as a promising diagnostic tool for substitution (Atkinson and Lennon, 2003; Legome and Pancu, 2004; McManus *et al.*, 2008).

1.2 Bone fractures and fracture healing process

Bones provide the mechanical support for the body. They are different in shapes and can be categorized as long bones, short bones, flat bones, irregular bones, sesamoid bones, and accessory bones (Martini *et al.*, 2005). There are two basic types of bone in the human skeleton. The outer surface of the long bone such as femur, tibia and humerus is coated with dense cortical bone, while spongy cancellous bone locates at the ends of the long bones and in the axial skeleton. Bovine long bones have similar structures to human long bones, except a thicker cortex. A cross sectional image of a long bovine bone is shown in Figure 1.1.

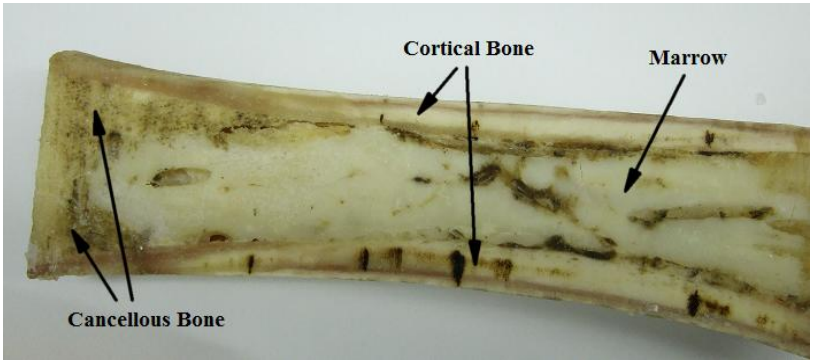

Figure 1.1: A cross section of a bovine long bone.

There are two different mechanisms for bone fracture (Doblar *et al.*, 2004; Gupta and Zioupos, 2008). The first mechanism appears when accidental loads on the bone exceed a certain threshold. This may happen through a fall or a sudden muscular contraction of elderly people with osteoporosis, a disease that will decrease bone mass and deteriorate micro-architecture of bone tissues. The other type of fracture happens due to creep or fatigue. Bones may produce micro-cracks when constant or cyclic loads are applied for prolonged periods of time. Bones can also repair such micro-fractures by bone remodeling. However, if the micro-damage accumulates faster than the repairing, micro-cracks will be deteriorated to produce macro-cracks resulting in fractures.

Fracture healing is a complex and dynamic regenerative process that gradually restores the structural integrity and mechanical function of the bone. Fracture healing can be divided into two major categories: primary bone healing and secondary bone healing (Phillips, 2005; Schindeler *et al.*, 2008). Primary bone healing is also called direct or cortical bone healing, which requires rigid

stabilization of the bone ends. As a result, it is rare in real cases, since most fractures occurring, either treated or untreated, will cause motion to some degree. It is the secondary bone healing that is most common in the repairing process. Secondary bone healing is characterized by spontaneous fracture healing without rigid fixation of the fracture site. The bone healing process has three overlapping phases: inflammatory phase, reparative phase, and remodeling phase (Dimitriou *et al.*, 2005; Phillips, 2005). The first phase starts immediately after bone fracture. The fracture gap is quickly filled with blood from hemorrhage, dead tissue is removed, and initial callus is originated. In the next phase, callus is gradually filled with cartilage. After that, cartilage continues to ossify and is finally replaced by bone. A bony bridge surrounds the fracture gap so that the fracture can be completely stabilized. Bone remodeling may last much longer time than the previous two phases, in which the original structure and shape of the bone is restored. In general, fracture healing can be completed in 6-8 weeks after the initial injury.

1.3 Diagnosis of fracture and monitoring methods for fracture healing

The universally adopted method in diagnosis of fractures is radiography, which will show the status of bone fracture in an X-ray image. Over the years, researchers have tried to involve ultrasound in the fracture diagnosis process, especially for fractures in children. Not only is ultrasound free of ionizing

radiation, but also it is an important complementary approach to X-ray because X-ray is not perfectly correct in the diagnosis. Controlled experiments have been carried out by researchers to detect fractures in children using both ultrasound and X-ray (Moritz *et al.*, 2008). Results showed that the sensitivity was 92.9% for ultrasound and 93.2% for X-ray, and ultrasound was superior to X-ray on detecting clavicle fracture. Although different sensitivity values were obtained by several groups (Ackermann *et al.*, 2009; Weinberg *et al.*, 2010), they have unanimously come to a conclusion that ultrasound is a valuable and safe alternative to X-ray in the diagnosis of bone fractures. For children with trauma, ultrasound was even proposed to be the imaging method of choice. If compound fracture exists, X-ray should be used to scan the region of interest predefined by ultrasound (Hubner *et al.*, 2000; Moritz *et al.*, 2008; Ackermann *et al.*, 2009), which will certainly reduce the radiation exposures.

In an attempt to apply ultrasound to diagnose fractures, standard medical phased array ultrasound scanners were used with frequency ranging from 5-10 MHz. Typical images obtained are shown in Figure 1.2. Figure 1.2(a1) is the image of a fractured turkey leg bone in an *in-vitro* study, while (a2) and (a3) are the sonographs of the bone in the longitudinal and cross-sectional directions respectively (Heiner and McArthur, 2009). Figure 1.2(b) and (c) are the *in-vivo* radiograph and sonograph of a fractured distal radius of a nine-year-old boy respectively (Hubner *et al.*, 2000). We can see that the *in-vitro* images in Figure

1.2(a) are much clearer than the *in-vivo* image in Figure 1.2(c) due to the soft tissue diffractions in the *in-vivo* measurement. In all the experiments taken above, either *in-vivo* or *in-vitro*, knowledge in ultrasound physics and experience in operating ultrasound scanners are required. Without any knowledge about medical ultrasound, it is hard to interpret the sonographs. Also, ordinary sonograph will not provide the geometry of the internal structure because they are the signals in time domain (depth axis with a constant velocity of tissue). Even with the *in-vitro* case shown in Figure 1.2(a), we can tell there are fractures in bone, but the fracture positions might not be correctly imaged.

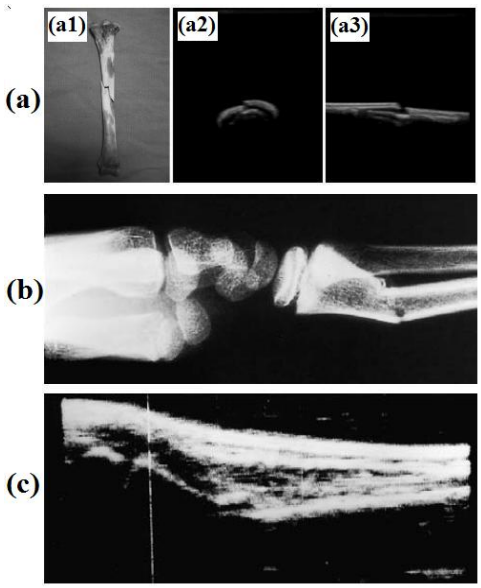

Figure 1.2: Images of fractured bones. (a) Sonograph of a fractured turkey leg bone (*in-vitro* study) (Heiner and McArthur, 2009); (b) Radiograph of a fractured distal radius of a nine-year-old boy; (c) The sonograph of the fracture shown in (b) (Hubner *et al.*, 2000).

In clinical studies, conventional radiography is perhaps the gold standard to assess fracture healing. For years, researchers have developed many other ways to monitor the healing process. They are dual energy X-ray absorptiometry (DXA), quantitative computed tomography (QCT), vibration analysis, and biomechanical testing (Morshed *et al.*, 2008). DXA provides an accurate method of quantifying the changes in bone mineral density (BMD), which occurs during fracture healing (Cattermole *et al.*, 1996; Blokhuis *et al.*, 2000). QCT has expanded the benefits of computed tomography and is able to image structures more accurately than conventional radiography especially in assessing metaphyseal and periarticular fractures. Besides imaging, QCT will provide a quantitative assessment of callus volume as well as bone density (Augat *et al.*, 1997; Fardellone, 2008). Vibration analysis works by measuring the resonant frequencies of a vibration pulse which transmits across the fracture. Resonant frequencies are then analyzed to get bending rigidity and torsion stiffness, parameters that are related to fracture mechanical properties (Nakatsuchi *et al.*, 1996). Biomedical testing truly measures the stiffness and strength in bending and torsion. However, it requires the removal of the fixation device and may cause pain to the patient (Moorcroft *et al.*, 2001; Matsuyama *et al.*, 2008).

Ultrasonography was also applied at the beginning of the healing process (six to nine weeks) when X-ray could not detect the non-ossified callus formed in the first stage of healing (Maffulli and Thornton, 1995; Moed *et al.*, 1998; Craig *et*

al., 1999). There was 97% success rate in predicting the status of union in a study involving 47 patients with tibial fracture (Moed *et al.*, 1998). To obtain a quantitative measurement of the fracture healing, computerized sonometry, a technique based on ultrasound axial transmission across a bone fracture is used (Morshed *et al.*, 2008). Typically, an ultrasound transmitter and receiver were placed on each side of the fracture, directly contacting with the skin, as shown in Figure 1.3 (Protopappas *et al.*, 2008). Then the velocity of ultrasound propagating from the transmitter to the receiver through the fracture part was measured, which could be compared with baseline measurement on an intact bone. The measurement result would determine the stage of the healing process. Apart from velocity, other parameters, such as fracture transmission loss and signal attenuations, were also simulated and experimentally measured to assess bone strength and monitor fracture healing (Dodd *et al.*, 2007a; Dodd *et al.*, 2007b; Dodd *et al.*, 2008).

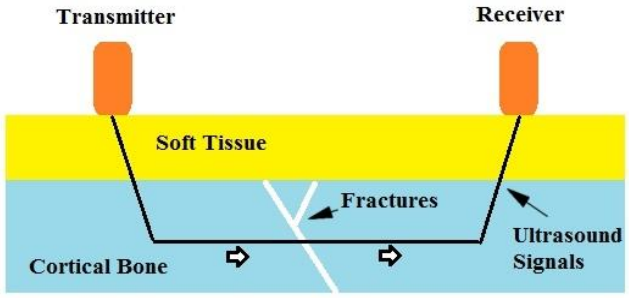

Figure 1.3: A schematic diagram of using axial transmission technique to evaluate fracture healing in long bone.

Another method to use ultrasound in monitoring bone fracture healing is based on guided waves (Prosser *et al.*, 1999). Developed for nondestructive evaluation (NDE) of engineering materials, the guided wave method analyzes ultrasound data to obtain different guided wave modes. The modes for fractured and intact bones were measured and compared for the healing status (Protopappas *et al.*, 2006; Protopappas *et al.*, 2007; Gheduzzi *et al.*, 2009).

1.4 Imaging methods in geophysics

Seismic imaging methods, such as travel-time tomography, diffraction tomography and seismic migration, are methodologies to obtain detailed images of the Earth's subsurface structures. Seismic migration is the most commonly used tool to image the Earth's structure. It is a process of mathematically transforming the observed data, which is acquired on the Earth's surface by seismometers or geophones, into images of the subsurface structures. In case of offshore, acquisition hydrophones will be used. The imaging process will transform or "migrate" the seismic events to their correct spatial locations by refocusing the diffraction energies back to their scattering sources.

In some sense, seismic modeling and seismic imaging are inverses of each other (Santos *et al.*, 2000). Modeling describes the forward process of generating observed data given an Earth model, showing seismic waves propagating from sources to scatterers, then from scatterers to receivers. While imaging, on the

other hand, attempts to undo the wave propagation effects to produce a model of the Earth (Gray *et al.*, 2001), which is the inverse of forward modeling.

Migration backprojects the scattered wavefields into the Earth backward in time to find where they were generated. Implemented as early as 1920s, migration techniques have been developed into a variety of seismic tools to image complex structures, in time and space, in two and three dimensions, pre-stack and post-stack, etc. Time migration moves events to the correct time, but it does not provide a correct geometrical model of the subsurface structures. Depth migration requires some knowledge about the Earth's velocity structure to find locations of the reflectors. Post-stack migration uses zero-offset data (data acquired with source and receiver at the same position) or stacked data. Post-stack migration is computationally fast but may deteriorate image quality because of the loss of information in the stacking procedure. As computers become faster, pre-stack migration using offset data (data acquired with source and receiver at different position) has become more and more popular. It requires no stacking of data, provides better image of the subsurface but it is more time consuming.

Migration techniques can be divided into two categories: ray-based migration and wave-equation based migration. Kirchhoff migration is the dominant procedure in ray-based migration (Schneider, 1978; Fehler and Huang, 2002). It is widely used in industry because of low computational cost. It is generally a high-frequency approximation using primary signals. The other secondary signals, such

as multiple reflections, will negatively affect the accuracy of the imaging results and will therefore be ignored in the imaging process. Wave-equation based migration (Claerbout, 1985) uses all wavefields to image the interior structure of the Earth. It is generally more accurate than ray-based Kirchhoff migration because there is no high frequency approximation and all primary and secondary arrivals are automatically considered.

Wave-equation migration consists of two steps: downward continuation of the recorded wavefields into the Earth and application of imaging condition (Claerbout, 1985; Fehler and Huang, 2002). Finite difference (FD) and Fourier transform (FT) are two major numerical techniques to downward propagate the wavefields. In the FD-based algorithms, there are finite difference migration, which is a downward continuation in depth (Claerbout, 1985; Mufti *et al.*, 1996), and reverse time migration (RTM), which is a downward continuation in time (Baysal *et al.*, 1983; McMechan, 1983; Whitmore, 1984; Bording and Lines, 1997). Finite difference migration uses one-way wave-equation and considers only the primary reflections for imaging. The RTM, on the other hand, uses the two-way wave equation, considers all wavefields and has the advantage of handling all dip angles. In FT-based algorithm, the derivatives in the wave-equations are calculated in the frequency-space or frequency-wavenumber domain, rather than in a time-space domain. The FT-based migration methods, such as phase-shift migration (Gazdag, 1978; Gazdag and Sguazzero, 1984a), phase-shift

plus interpolation migration (Gazdag and Sguazzero, 1984b), and split-step Fourier migration (SSFM) (Stoffa *et al.*, 1990; Huang *et al.*, 1999), can minimize the artificial numerical dispersion effects commonly occurred in FD-based methods, and have the advantage of fast computational speed because of the fast FT (FFT) algorithm. However, approximations about the velocity variations such as ignoring the lateral velocity change are made in these methods, which may affect the migrated image quality. There are also hybrid migration methods, such as the Fourier FD method (Ristow and Ruhl, 1994), which has the advantages of both the FD and FT based algorithms.

The imaging condition specifies where the reflectors are located in the subsurface. A commonly used imaging condition is a cross-correlation method, which is assessed by cross-correlating the source wavefields and receiver wavefields and summing over all sources (Claerbout, 1971). More technical details will be provided in Chapter 2.

1.5 Application of imaging methods in other areas

Beyond geophysics, researchers have extended the application of migration imaging methods to other areas, such as material testing and medicine. Nondestructive evaluation (NDE) techniques, which are used to detect anomalies in materials or work pieces, take the advantages of ultrasound, such as deep penetration and high resolution, in material testing. For NDE, researchers have attempted to use Kirchhoff migration and frequency wavenumber migration,

developed in the field of reflection seismology, to image embedded cracks and holes in concrete structures (Chang and Chern, 2000; Chang *et al.*, 2001; Chang and Ton, 2001). In medical imaging, researchers have been exploring the application of wave-equation migration to image breast tissues (Huang *et al.*, 2003). They tried RTM, SSFM and Fourier finite-difference migration and achieved better imaging results than conventional sonography (Huang *et al.*, 2006; Huang and Quan, 2007; Huang *et al.*, 2008).

The idea of reversing the time series also applies in other areas besides geophysics. Time reversal mirror (TRM), a concept introduced by Fink et al. (Fink *et al.*, 1989), and widely researched in medicine for years (Derode *et al.*, 1995; Fink *et al.*, 2003; Fink, 2006; Bavu *et al.*, 2007; Fink *et al.*, 2009), is an example. TRMs are used to focus wavefields through inhomogeneous media on a reflective target. A TRM consists of one- or two-dimensional transducer array, with each element connected to its own electronic circuitry. The circuitry includes a receiving amplifier, an A/D converter, storage memory and a programmable transmitter able to synthesize time-reversed version of the signals stored in the memory (Wu *et al.*, 1992). The focusing process requires three steps. In the first step, the transmitter array illuminates the wavefields through the inhomogeneous medium to the target. The echoes from the target are distorted or modulated by the medium and recorded by the array in the second step. In the last step, the transducer array synthesizes the time reversed wavefields, which propagate

through the medium and are focused on the target (Fink, 1992). Iterative time-reversal process can be used if the target is spatially extended or there are several targets to focus. The TRM techniques have been applied to medicine in lithotripsy, stone destruction, and trans-skull brain therapy, etc (Fink *et al.*, 2003). Besides medicine, time reversal acoustics have been applied in nondestructive testing (NDT) (Claire, 2002; Chun, 2004) and signal communications (Heinemann *et al.*, 2003; Edelmann *et al.*, 2005).

The RTM and Fink's TRM method are closely related. They both take the advantage of time reversal invariance of the acoustic wave equation to obtain images of reflectors in the medium. Through the images, the position of the anomalies and reflecting strength can be determined. The RTM achieves the reconstruction of the image in a virtual way. In other words, the image is reconstructed via a computational process, not through measurement. While for the TRM method, a real measurement is needed to detect the reemitted time-reversed signals and find the point with the strongest pressure, where the anomalies should locate. The RTM is used to obtain the whole image of the subsurface layers, while the TRM performs better in locating anomalies through non-uniform medium. For the purpose of imaging bone fracture structure, the RTM is more appropriate, since we need to image the reflecting surfaces, not localized anomalies and the measurement can be much faster.

1.6 Motivation

As being mentioned above, X-ray based technologies are the gold standard to image bone fractures in clinical application. The X-ray technique has the advantage of high resolution and fast imaging. However, ionizing radiation in the X-ray testing is harmful to patients, especially when long imaging or scanning time is required, such as CT. Moreover, X-ray devices are large and expensive, and professional training is required before using them. Magnetic Resonance Imaging (MRI) technique is an alternative to eliminate radiation, but it is much more expensive and time consuming for imaging bone fractures. Ultrasound, on the other hand, is a radiation-free technique and has been widely used in medical imaging, especially in soft tissues. Medical ultrasound scanners are small and portable. They are easy to use and affordable. To reduce radiation exposure to patients especially children and the medical expenses, we here present a method of using ultrasound to image bone fractures and to monitor the fracture healing process. Although some attempts have been made to use B-mode medical ultrasound to image bone fracture; the resulting images do not provide correct geometrical and structural information of the fractures. The use of seismic migration techniques has the potential to overcome this shortcoming and to reconstruct a more detailed image of the bone structure.

1.7 Thesis overview

In Chapter 2, we introduce the relevant imaging theories. Exploding reflector model will be introduced as the basic model for zero-offset imaging. Reverse-time imaging and split step imaging will be discussed respectively.

In Chapter 3, numerical simulations will be carried out using some simple bone models. We establish a stratified bone model to mimic long bones. Fractures in bones are also simplified to have regular shapes, in order to make easy comparisons between different cases. We demonstrate the ability of the migration methods in determining cortical bone thickness. Fractures with different dip angles are also reconstructed using migration. Noises are added to test the robustness of the method. In order to obtain more accurate images, iterative migration method is applied. At the end, we also introduce a possible way to detect fracture healing process using migration. In the numerical simulations, both RTM and SSFM methods are used and comparisons of the results will be shown for each case.

Chapter 4 shows the application of migration to real data. We acquire data from a Plexiglas phantom, a deer cortical bone plate and a bovine long bone. The recorded signals are filtered, amplified and interpolated before being migrated. SSFM is used to focus the reflections to the exact positions where they originate. The reconstructed image presents the structural information of the tested samples. Some possible ways to obtain better experimental results are also discussed.

Chapter 5 will summarize the thesis and conclude the possibility of using migration imaging techniques to detect bone structures.

Chapter 2. Theory of wave equation migration

2.1 Introduction

The propagation of elastic waves is mathematically represented by the wave equation. In the imaging process, we attempt to achieve two goals. One is to locate the reflectors by back-propagating the wavefields recorded on the surface of the sample and the other is to retrieve the amplitude during the back propagation to estimate the reflection coefficients of the reflectors. In wave equation migration, one can either use the one-way or two-way wave equation. The one-way wave equation propagates energy in one direction, usually downward. It is superior to ray-based migration if multi-path exists such as surrounding salt bodies (Operto *et al.*, 2000; Mulder and Plessix, 2004), but the method is not so accurate when the structure has sharp lateral velocity changes, steep slopes or dips (Albertin *et al.*, 2002). The two-way wave equation migration, also called full wave equation migration, can describe wave propagation more accurately in a complex medium. Unlike the one way wave equation, it generally has no dip limitations, but the computational cost is larger; however the computational cost is not so much for two-dimensional (2D) cases (Mulder and Plessix, 2004).

2.2 Acoustic wave equation

In a lossless three-dimensional (3D) medium, the linearized equation of motion in Cartesian coordinate is given by

$$\rho \frac{\partial^2 u_i}{\partial t^2} = \sum_{j=1}^{3} \frac{\partial \tau_{ij}}{\partial x_j} \quad (i = 1,2,3) \tag{2.1}$$

where $u_i = u_i(\mathbf{x}, t)$ is the particle displacement in the ith direction, which is a function of position $\mathbf{x}$ and time t, $\tau_{ij} = \tau_{ij}(\mathbf{x}, t)$ is the stress tensor representing the jth component of the traction acting across the plane normal to the ith axis, and ρ is the material density, which is spatially varying.

For an isotropic medium, the stress-displacement equation is:

$$\tau_{ij} = \tau_{ji} = \lambda \delta_{ij} \nabla \cdot \mathbf{u} + 2\mu \varepsilon_{ij}, \tag{2.2}$$

where δ_{ij} is the Kronecker delta, λ and μ are the position-dependent Lamé constants (Wapenar and Berkhout, 1989). The divergence is $\nabla \cdot \mathbf{u} = \sum_{i=1}^{3} \partial u_i / \partial x_i$ and the stain tensor ε_{ij} is

$$\varepsilon_{ij} = \frac{1}{2}\left(\frac{\partial u_i}{\partial x_j} + \frac{\partial u_j}{\partial x_i} \right). \tag{2.3}$$

The bulk compression modulus $K(\mathbf{x})$ and the bulk shear modulus $G(\mathbf{x})$ are related to the Lamé constants by

$$K(\mathbf{x}) = \lambda(\mathbf{x}) + \frac{2}{3}\mu(\mathbf{x}) \tag{2.4a}$$

and

$$G(\mathbf{x}) = \mu(\mathbf{x}). \tag{2.4b}$$

In an isotropic acoustic medium, the shear stress components in the stress tensor reduce to zero due to $\mu = 0$ and $\lambda = K$. Equation (2.2) can be simplified to

$$\tau_{ii} = K\nabla \cdot \mathbf{u} \quad (i = 1,2,3). \tag{2.5}$$

Substituting equation (2.5) into equation (2.1), yields

$$\rho \frac{\partial^2 \mathbf{u}}{\partial t^2} = K\nabla^2 \mathbf{u}. \tag{2.6}$$

where ∇^2 is the Laplacian operator.

For a 2D isotropic medium with the source term added, equation (2.6) will turn into what is called the Helmoholtz wave-equation:

$$\frac{1}{c(\mathbf{x})^2}\frac{\partial^2}{\partial t^2} u(\mathbf{x}, \mathbf{x}_s, t) = \nabla^2 u(\mathbf{x}, \mathbf{x}_s, t) + f(t)\delta(\mathbf{x} - \mathbf{x}_s), \tag{2.7}$$

where $u(\mathbf{x}, \mathbf{x}_s, t)$ is the acoustic wave-field at position $\mathbf{x}$ due to the source located at $\mathbf{x}_s$ at time *t*, $c(\mathbf{x}) = \sqrt{K(\mathbf{x}) \big/ \rho(\mathbf{x})}$ is the spatially varying phase velocity, $f(t)$ is the source function at time *t*, located at $\mathbf{x}_s$, and δ is the Kronecker delta.

2.3 Linear scattering theory

Due to the spatially varying velocity, it is difficult to solve directly the nonlinear equation shown in equation (2.7). As a result, a linearization procedure is seeked

to simplify this problem. The Born approximation is commonly used to linearize the nonlinear wave equation by decomposing the nonlinear term to a sum of background and perturbation components based on the assumption that the perturbation is much smaller than the background contribution.

In order to derive the scattering wavefields and compute the forward signals, we first Fourier-transform equation (2.7) as

$$\left(\nabla^2 + \frac{\omega^2}{c(\mathbf{x})^2}\right) u(\mathbf{x}, \mathbf{x}_s, \omega) = -F(\omega)\delta(\mathbf{x} - \mathbf{x}_s) \tag{2.8}$$

where $F(\omega)$ is the Fourier representation of the source function at the angular frequency ω. Define the acoustic velocity potential $\alpha(\mathbf{x})$ as

$$\alpha(\mathbf{x}) = \frac{1}{c(\mathbf{x})^2} - \frac{1}{c_0(\mathbf{x})^2} \tag{2.9}$$

where $c_0(\mathbf{x})$ is the constant background velocity. Substituting equation (2.9) into equation (2.8), yields

$$\nabla^2 u(\mathbf{x}, \mathbf{x}_s, \omega) + \frac{\omega^2}{c_0(\mathbf{x})^2} u(\mathbf{x}, \mathbf{x}_s, \omega) = -F(\omega)\delta(\mathbf{x} - \mathbf{x}_s) - \omega^2 \alpha(\mathbf{x}) u(\mathbf{x}, \mathbf{x}_s, \omega). \tag{2.10}$$

The Green's function G_0 satisfies the wave equation with a background velocity:

$$\nabla^2 G_0(\mathbf{x}, \mathbf{x}_s, \omega) + \frac{\omega^2}{c_0(\mathbf{x})^2} G_0(\mathbf{x}, \mathbf{x}_s, \omega) = -\delta(\mathbf{x} - \mathbf{x}_s). \tag{2.11}$$

As a result, based on the Green's theorem, the total wavefields at receiver point $\mathbf{x}_r$ are a combination of the background wavefields and the scattered wavefields (Taylor, 1972):

$$u(\mathbf{x}_r, \mathbf{x}_s, \omega) = G_0(\mathbf{x}_r, \mathbf{x}_s, \omega)F(\omega) + \omega^2 F(\omega)\int G_0(\mathbf{x}_r, \mathbf{x}, \omega)\alpha(\mathbf{x})u(\mathbf{x}, \mathbf{x}_s, \omega)d\mathbf{x}, \quad (2.12)$$

where $G_0(\mathbf{x}_r, \mathbf{x}_s, \omega)$ is the background wavefield and the latter part is the scattered wavefield, which is an integration over the scattered volume. So we have changed the differential equation (2.10) into an integral equation (2.12).

The scattered wavefields u_{sc} can be written as:

$$u_{sc}(\mathbf{x}_r, \mathbf{x}_s, \omega) = \omega^2 F(\omega)\int G_0(\mathbf{x}_r, \mathbf{x}, \omega)\alpha(\mathbf{x})u(\mathbf{x}, \mathbf{x}_s, \omega)d\mathbf{x} \quad (2.13)$$

which is still hard to solve since the total wavefield is not known. The first order Born approximation states that if the scattered wavefield is small, i.e., $u_{sc} << u$, the total wavefield can be replaced by background wavefield, which means $u \approx G_0$. As a result, the scattered wavefield can be linearized as follows:

$$u_{sc}(\mathbf{x}_r, \mathbf{x}_s, \omega) = \omega^2 F(\omega)\int G_0(\mathbf{x}_r, \mathbf{x}, \omega)\alpha(\mathbf{x})G_0(\mathbf{x}, \mathbf{x}_s, \omega)d\mathbf{x}. \quad (2.14)$$

We write the Green's function as a wave propagation between any two arbitrary points (Beylkin, 1985):

$$G_0(\mathbf{x}, \mathbf{y}, \omega) = A(\mathbf{x}, \mathbf{y})e^{i\omega\tau(\mathbf{x},\mathbf{y})} \quad (2.15)$$

where $A(\mathbf{x},\mathbf{y})$ is the amplitude of the ray that travels from $\mathbf{x}$ to $\mathbf{y}$ and $\tau(\mathbf{x},\mathbf{y})$ is the travel time for the wave to propagate between the two positions. The amplitude and the travel time for a ray to travel from a fixed position $\mathbf{y}$ to any position $\mathbf{x}$ satisfy the transport equation and eikonal equation, respectively:

$$A(\mathbf{x},\mathbf{y})\nabla_{\mathbf{x}}^2\tau(\mathbf{x},\mathbf{y}) + 2\nabla_{\mathbf{x}}\tau(\mathbf{x},\mathbf{y})\cdot\nabla_{\mathbf{x}}A(\mathbf{x},\mathbf{y}) = 0 \tag{2.16a}$$

and

$$|\nabla_{\mathbf{x}}\tau(\mathbf{x},\mathbf{y})|^2 = \frac{1}{c_0(\mathbf{x})^2} \tag{2.16b}$$

where ∇ is the gradient operator. By substituting equation (2.15) into equation (2.14), the scattered wavefields will be written as

$$u_{sc}(\mathbf{x}_r,\mathbf{x}_s,\omega) = \omega^2 F(\omega)\int A(\mathbf{x}_r,\mathbf{x})e^{i\omega\tau(\mathbf{x}_r,\mathbf{x})}\alpha(\mathbf{x})A(\mathbf{x},\mathbf{x}_s)e^{i\omega\tau(\mathbf{x},\mathbf{x}_s)}d\mathbf{x}. \tag{2.17}$$

If we define the amplitude and travel time for the incident and scattered wavefields respectively as

$$A(\mathbf{x}_r,\mathbf{x},\mathbf{x}_s) = A(\mathbf{x}_r,\mathbf{x})A(\mathbf{x},\mathbf{x}_s) \tag{2.18a}$$

and

$$\tau(\mathbf{x}_r,\mathbf{x},\mathbf{x}_s) = \tau(\mathbf{x}_r,\mathbf{x}) + \tau(\mathbf{x},\mathbf{x}_s), \tag{2.18b}$$

then equation (2.17) becomes

$$u_{sc}(\mathbf{x}_r,\mathbf{x}_s,\omega) = \omega^2 F(\omega)\int A(\mathbf{x}_r,\mathbf{x},\mathbf{x}_s)e^{i\omega\tau(\mathbf{x}_r,\mathbf{x},\mathbf{x}_s)}\alpha(\mathbf{x})d\mathbf{x}. \tag{2.19}$$

Using inverse Fourier transform, equation (2.19) can be transformed into time domain,

$$u_{sc}(\mathbf{x}_r,\mathbf{x}_s,t)=\left[-\frac{\partial^2}{\partial t^2}\int A(\mathbf{x}_r,\mathbf{x},\mathbf{x}_s)\delta\left(t-\tau(\mathbf{x}_r,\mathbf{x},\mathbf{x}_s)\right)\alpha(\mathbf{x})d\mathbf{x}\right]* f(t), \quad (2.20)$$

where the symbol $*$ represents convolution. The second order derivative in equation (2.20) can be shifted to the source wavelet as follows (Tarantola, 1984):

$$u_{sc}(\mathbf{x}_r,\mathbf{x}_s,t)=\left[-\int A(\mathbf{x}_r,\mathbf{x},\mathbf{x}_s)\delta\left(t-\tau(\mathbf{x}_r,\mathbf{x},\mathbf{x}_s)\right)\alpha(\mathbf{x})d\mathbf{x}\right]*\frac{\partial^2}{\partial t^2} f(t). \quad (2.21)$$

In the 2D case, the Green's function for any points in the far field ($\omega\tau(\mathbf{x},\mathbf{y})>>1$) is given by (Beylkin, 1985; Miller *et al.*, 1987):

$$G_0(\mathbf{x},\mathbf{y},\omega)=(-i\omega)^{-1/2}A(\mathbf{x},\mathbf{y})e^{i(\omega\tau(\mathbf{x},\mathbf{y})+\pi/4)} \quad (2.22)$$

where

$$A(\mathbf{x},\mathbf{y})=\left(\frac{c_0}{8\pi\,|\mathbf{x}-\mathbf{y}|}\right)^{1/2}. \quad (2.23)$$

As a result, equation (2.19), (2.20), and (2.21) can be simplified as:

$$u_{sc}(\mathbf{x}_r,\mathbf{x}_s,\omega)=i\omega f(\omega)\int A(\mathbf{x}_r,\mathbf{x},\mathbf{x}_s)e^{i\omega\tau(\mathbf{x}_r,\mathbf{x},\mathbf{x}_s)}\alpha(\mathbf{x})d\mathbf{x}, \quad (2.24a)$$

$$u_{sc}(\mathbf{x}_r,\mathbf{x}_s,t)=\left[\frac{\partial}{\partial t}\int A(\mathbf{x}_r,\mathbf{x},\mathbf{x}_s)\delta\left(t-\tau(\mathbf{x}_r,\mathbf{x},\mathbf{x}_s)\right)\alpha(\mathbf{x})d\mathbf{x}\right]* f(t),$$

or

$$u_{sc}(\mathbf{x}_r,\mathbf{x}_s,t)=\left[\int A(\mathbf{x}_r,\mathbf{x},\mathbf{x}_s)\delta\left(t-\tau(\mathbf{x}_r,\mathbf{x},\mathbf{x}_s)\right)\alpha(\mathbf{x})d\mathbf{x}\right]*\frac{\partial}{\partial t} f(t), \quad (2.24b)$$

where

$$A(\mathbf{x}_r,\mathbf{x},\mathbf{x}_s)=\frac{c_0}{8\pi}\left(\frac{1}{|\mathbf{x}_r-\mathbf{x}\|\mathbf{x}-\mathbf{x}_s|}\right)^{1/2}. \quad (2.25)$$

Equations (2.24) are the basics for computing the scattered signals in the linear Born scattering theory.

2.4 Reverse time migration (RTM)

2.4.1 Exploding reflector model

The exploding reflector model (Loewenthal *et al.*, 1976), can help us understand the concept of migration for zero-offset or post-stack data. According to this model, the acoustic waves emanated from a source, travel through the medium at velocity *v*. After being reflected at an interface, part of the waves will travel back along the initial path to the receiver located at the same position as the source. Alternatively, according to the Huygens' principle, we can consider the reflected waves to be generated by a series of point explosions along the reflecting surface at time zero and travel one way to the recording surface at half velocity *v*/2. For the zero-offset case, where source and receiver are at the same position, the exploding reflector response is considered equivalent to the wavefield propagating downward from the source to the reflector and then back to the receiver along the same path at the medium's velocity.

2.4.2 Zero-offset reverse time migration

By using the exploding reflector model, researchers explained the idea of RTM through a point diffractor example, as shown in Figure 2.1 (McMechan, 1983). This figure shows the snapshots of wavefield for a point diffractor at times

$t = 0,\ t = t_j$ and $t = t_i$, respectively. The signal recorded on the surface is shown on the top displaying an expected diffraction hyperbola. The reflection is obvious. In order to image the point diffractor, MeMechan reversed the time order of the recorded wavefields. By using this reversed wavefield as source, the signals are back propagated with half the medium velocity to time zero, when the wavefield shows the exact position and reflection strength of the point diffractor. This process has the same effect as running the wavefield movie backwards in time.

Due to Huygens' Principle, a seismic section can be considered as the superposition of responses from a set of point diffractors. So when it comes to a reflecting surface, the procedures are exactly the same.

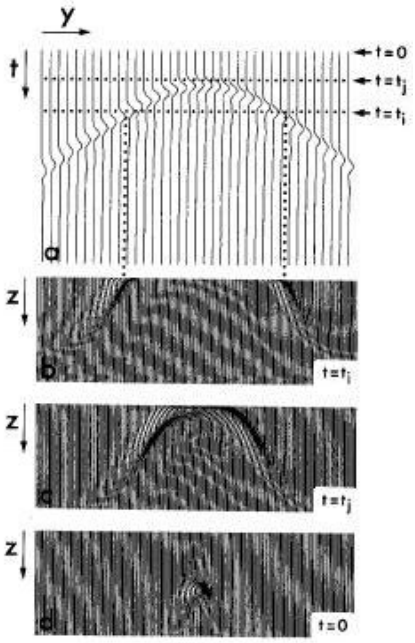

Figure 2.1: Reverse time migration (RTM) from a point diffractor model (McMechan, 1983).

An explicit FD approach is naturally applied to equation (2.7). Based on the second order centered FD operator in space-time (*x*-*t*), the equation is discretized as follows:

$$\left(\frac{u^n_{i_x-1,i_z}-2u^n_{i_x,i_z}+u^n_{i_x+1,i_z}}{(\Delta x)^2}\right)+\left(\frac{u^n_{i_x,i_z-1}-2u^n_{i_x,i_z}+u^n_{i_x,i_z+1}}{(\Delta z)^2}\right) -\frac{1}{c^2_{i_x,i_z}}\left(\frac{u^{n+1}_{i_x,i_z}-2u^n_{i_x,i_z}+u^{n-1}_{i_x,i_z}}{(\Delta t)^2}\right)=-f(n)\delta(x_{i_x}-x_s)\delta(z_{i_z}-z_s), \tag{2.26}$$

where Δx and Δz are the grid sizes in the *x* and *z* directions, Δt is the time step, the superscript *n* means the *n*th time step, while the subscripts i_x and i_z, are the index of the grid points in the *x* and *z* axes, and $f(n)$ is the source function at time step *n*.

From equation (2.26), we can derive the expression for the forward modeling procedure, using the wavefields at time step n and $n-1$ to obtain the wavefields at time step $n+1$:

$$u^{n+1}_{i_x,i_z}=2u^n_{i_x,i_z}-u^{n-1}_{i_x,i_z}+\left(\frac{c_{i_x,i_z}\Delta t}{h}\right)^2(u^n_{i_x+1,i_z}+u^n_{i_x-1,i_z}+u^n_{i_x,i_z+1}+u^n_{i_x,i_z-1}-4u^n_{i_x,i_z}) +f(n)\delta(x_{i_x}-x_s)\delta(z_{i_z}-z_s). \tag{2.27}$$

Notice that we take the increment in *x* and *z* direction the same, i.e., $\Delta x=\Delta z=h$. The condition for local stability of the FD approach is $h/\Delta t\geq\sqrt{2}c$, which means that the information cannot propagate across the mesh faster than the mesh velocity (Strikwerda, 1989). The first order absorbing boundary conditions are used in the model:

$$\left(\frac{\partial}{\partial \hat{n}} - \frac{1}{c(x,z)} \frac{\partial}{\partial t} \right) u = 0, \tag{2.28}$$

where $\hat{n}$ is the normal to the boundary. Also, to avoid aliasing effects, Nyquist criteria requires at least two grid points per wavelength (Liu, 1997).

For the RTM, the procedure is almost the same, except in this case, we should reverse the time backward. The wavefields at time step *n* and *n*+1 are used to deduce the wavefields at *n*-1, i.e.,

$$\begin{aligned} u_{i_x,i_z}^{n-1} = {} & 2u_{i_x,i_z}^{n} - u_{i_x,i_z}^{n+1} + \left(\frac{c_{i_x,i_z} \Delta t}{h} \right)^2 (u_{i_x+1,i_z}^{n} + u_{i_x-1,i_z}^{n} + u_{i_x,i_z+1}^{n} + u_{i_x,i_z-1}^{n} - 4u_{i_x,i_z}^{n}) \\ & + g(n)\delta(x_{i_x} - x_r)\delta(z_{i_z} - z_r), \end{aligned} \tag{2.29}$$

where $g(n)$ is the wavefields recorded by the receivers at time step *n*. The velocity c_{i_x,i_z}, an input for the migration procedure, is a preliminary assumption of the velocity model, which is required to be smooth and can be refined in an iterative process (Whitmore, 1984). Remember that only half the medium velocity will be needed according to the exploding reflector model. The stability conditions mentioned above are still required in migration. The imaging condition for the zero-offset case is simply achieved when the time equals to zero (Baysal *et al.*, 1983). So when time is extrapolated to time zero, the wavefields will give us the information of the reflecting surface.

The application of RTM to the pre-stack data is different from that for the post-stack (zero-offset) data set. Time extrapolation of the received data is still

required. However, in the pre-stack case, the exploding reflector model will no longer apply, so the wavefields will be back propagated to original time using full assumed velocity model. And the imaging condition will be achieved by cross-correlating the source wavefields and receiver wavefields and summed over all sources (Bording and Lines, 1997),

$$I(z,x) = \sum_{s}\sum_{t} S_s(x,z;t)R_s(x,z;t). \tag{2.30}$$

The computing flow chart is shown in Figure 2.2.

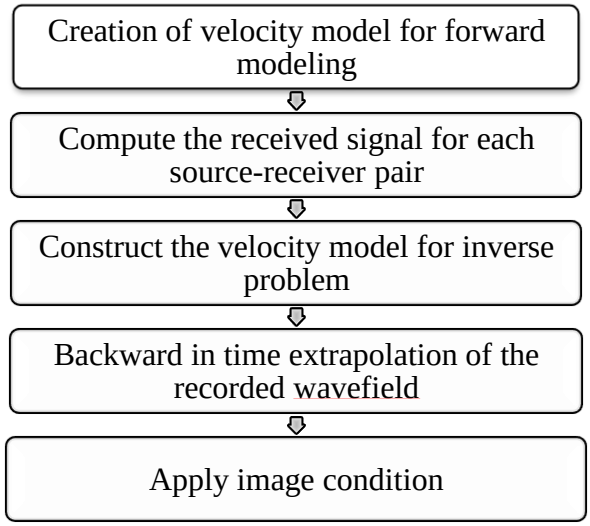

Figure 2.2: Flow chart for forward modeling and reverse time migration.

2.5 Split step Fourier migration (SSFM)

Because of the three different loops with respect to *x*, *z*, and *t* in the migration process, the RTM, although accurate in imaging, can take a long computational time. SSFM, on the other hand, is also a wave equation based migration method

and has the ability to compute at a much faster speed, because the computing procedures are performed in the Fourier domain, thus eliminating the time consuming FD process.

SSFM was developed by researchers in 1990 (Stoffa *et al.*, 1990). The method takes into account the laterally varying velocity by defining a reference slowness as the mean slowness in the migration slowness interval and a perturbation term that is spatially varying with position. Slowness, s is the reciprocal of half of velocity c according to the exploding reflector model, i.e., $s = 2/c$. Following Stoffa's paper, the acoustic wave equation (2.7) can be written as

$$\nabla^2 p - s^2 \frac{\partial^2}{\partial t^2} p = 0 \tag{2.31}$$

where $p = p(\mathbf{x}, t)$ is the pressure wavefield. Here we neglect the source term in equation (2.7). By Fourier transforming in *t,* Equation (2.31) becomes

$$\nabla^2 P(\mathbf{r}, z, \omega) + \omega^2 s^2 P(\mathbf{r}, z, \omega) = 0 \tag{2.32}$$

where $\mathbf{r} = x\hat{\mathbf{i}} + y\hat{\mathbf{j}}$ is the horizontal position vector and $P(\mathbf{r}, z, \omega)$ is the FT of the wavefields $p(\mathbf{x}, t)$.

We further decompose the slowness $s(\mathbf{r}, z)$ into background and perturbation slowness:

$$s(\mathbf{r},z) = s_0(z) + \Delta s(\mathbf{r},z) \tag{2.33}$$

where $s_0(z)$ is defined as the reference slowness. All variations are accommodated by the $\Delta s(\mathbf{r},z)$ term. Substituting (2.33) into equation (2.32),

$$\nabla^2 P + \omega^2 {s_0}^2 P = -\omega^2 (2s_0 \Delta s + \Delta s^2) P. \tag{2.34}$$

If we define a term $S(\mathbf{r},z,\omega) = \omega^2 \left[2s_0 \Delta s(\mathbf{r},z) + \Delta s^2(\mathbf{r},z) \right] P(\mathbf{r},z,\omega)$, then equation (2.34) can be simplified as

$$\nabla^2 P(\mathbf{r},z,\omega) + \omega^2 {s_0}^2 P(\mathbf{r},z,\omega) = -S(\mathbf{r},z,\omega). \tag{2.35}$$

As a result, the inhomogeneity or perturbation in slowness will be included only in the source-like term $S(\mathbf{r},z,\omega)$.

The split step Fourier method can be used to solve equation (2.35) by ignoring the Δs^2 term in $S(\mathbf{r},z,\omega)$. The procedure is summarized in several steps as follows. First, FT the up-going wavefields at depth z_n, $P(\mathbf{r},z_n,\omega)$, from $\mathbf{r}$ to $\mathbf{k}_r$ space:

$$\tilde{P}(\mathbf{k}_r,z_n,\omega) = \int_{-\infty}^{+\infty}\int_{-\infty}^{+\infty} P(\mathbf{r},z_n,\omega) e^{i\mathbf{k}_r\cdot\mathbf{r}} dxdy, \tag{2.36}$$

where $\mathbf{k}_r = k_x\hat{\mathbf{i}} + k_y\hat{\mathbf{j}}$ is the horizontal wave vector. The second step is to apply a phase shift based on the vertical wavenumber using the reference slowness

$$\tilde{P}_1(\mathbf{k}_r,z_n,\Delta z,\omega) = \tilde{P}(\mathbf{k}_r,z_n,\omega) e^{i(k_z)_0 \Delta z}, \tag{2.37}$$

where

$$(k_z)_0 = \sqrt{\omega^2 s_0^{\,2} - k_r^{\,2}} = \omega s_0 \sqrt{1-(k_r / \omega s_0)^2} \tag{2.38}$$

and s_0 is the mean slowness for the interval between z_n and $z_n + \Delta z$. The next step is to inverse FT the phase shifted data $\tilde{P}_1(\mathbf{k}_r, z_n, \Delta z, \omega)$ back from $\mathbf{k}_r$ to $\mathbf{r}$:

$$P_1(\mathbf{r}, z_n, \Delta z, \omega) = \left(\frac{1}{2\pi}\right)^2 \int_{-\infty}^{+\infty}\int_{-\infty}^{+\infty} \tilde{P}_1(\mathbf{k}_r, z_n, \Delta z, \omega) e^{-i\mathbf{k}_r \cdot \mathbf{r}} dk_x dk_y. \tag{2.39}$$

Then a second phase shift due to the perturbation in the slowness is applied, that is $\Delta s(\mathbf{r}, z) = s(\mathbf{r}, z) - s_0(z)$ in the interval between z_n and $z_n + \Delta z$:

$$P(\mathbf{r}, z_{n+1}, \omega) = e^{i\omega \Delta s(\mathbf{r}, z)\Delta z} P_1(\mathbf{r}, z_n, \Delta z, \omega). \tag{2.40}$$

Then if we integrate $P(\mathbf{r}, z_{n+1}, \omega)$ over the frequency range of interest, the migrated data for the current depth will be obtained, i.e.,

$$u(\mathbf{r}, z_{n+1}, 0) = \left(\frac{1}{2\pi}\right)^2 \int_{\omega_2}^{\omega_1} P(\mathbf{r}, z_{n+1}, \omega) d\omega. \tag{2.41}$$

The steps iterate and we will obtain the wavefields at all the depth sections. The flow chart for SSFM is shown in Figure 2.3.

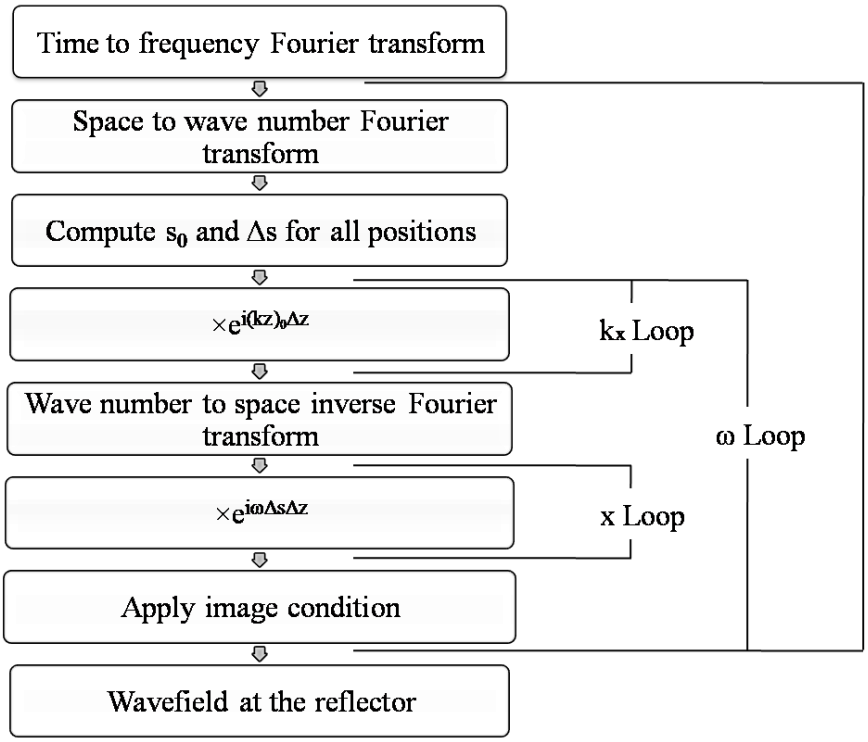

Figure 2.3: Flow chat for the split step Fourier migration (SSFM).

2.6 Summary

In this chapter, we introduced the basic theory of acoustic wave equation, RTM, and SSFM. Acoustic wave equation is derived directly from the equation of motion. The exploding reflector model is the basic assumption for the zero-offset RTM and one-way SSFM. RTM is achieved through the FD process, which is quite time consuming but can provide a more accurate reconstructed image, especially when the velocity is spatially dependent. SSFM, on the other hand, performs the reconstruction in the Fourier domain and works very fast. However,

because of the intrinsic assumption about the slowness, some artifacts in the reconstructed image will be expected in a complex velocity model.

As stated in the introduction, although these migration methods originated and have been actively applied in geophysics, applications of migration imaging in other areas are also being explored in recent years. In the next two chapters, we will use migration methods to image bone structures using simulated and experimental data sets.

Chapter 3. Imaging of long bones: a numerical study

In this chapter, we simulate ultrasound data to study the migration algorithms. We first use the migration methods to reconstruct an intact long bone image and estimate the thickness of the cortical layer. Then we change the intact models to fractured ones. Different fracture angles and fracture sizes are simulated. A possible process to determine fracture healing is also studied. In each case, both RTM and SSFM methods are used. While the former is accurate but time consuming, the latter one gives us a fast way to get a decent image.

3.1 Bone model for simulation

A cross-sectional X-ray computed tomographic (CT) image of a bovine tibia is shown in Figure 3.1. As stated in Chapter 1, a long bone is mainly composed of cortical bone in the outer part (white area in the mid shaft), marrow in the middle cavity (gray area), and cancellous bones (mainly at each end of the sample).

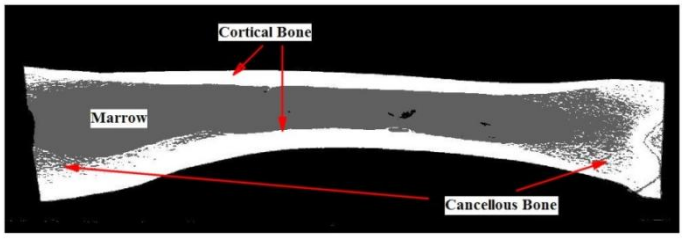

Figure 3.1: An X-ray CT image of a bovine tibia.

Cortical bone and marrow are two distinct materials and their ultrasound characteristic impedances Z are quite different. The characteristic impedance of a medium is defined by the product of its density, ρ and the speed of ultrasound, c within it, i.e.,

$$Z = \rho c \tag{3.1}$$

If the characteristic impedances of the two media are equal, there is no reflection and all the incident ultrasound energy is transmitted across the boundary. If the characteristic impedance differs, some of the energy is reflected. When a wave is incident normally on the interface separating two media, the fraction of the incident energy which is reflected is given by the reflection coefficient:

$$R = \left(\frac{Z_2 - Z_1}{Z_2 + Z_1} \right)^2 \tag{3.2}$$

where Z_1 and Z_2 are the characteristic impedances of medium 1 and medium 2 respectively. As a result, if Z_1 and Z_2 are very different and the contrast is large, almost total reflection will occur.

The ultrasound characteristic impedance of cortical bone and marrow are around $5 \times 10^6 kg/(m^2 s)$ and $1.5 \times 10^6 kg/(m^2 s)$ respectively. The soft tissue and marrow have similar impedance. This means only around 29% of the energy will be reflected from the cortical bone-marrow interface (Wells, 1983). Besides, absorption occurs when ultrasound travels in the bone. The primary reflections are

mainly from the first layer of the cortical bone (Le *et al.*, 2010). So in our theoretical model, we use a one layer cortical bone model to mimic the mid shaft of a long bone.

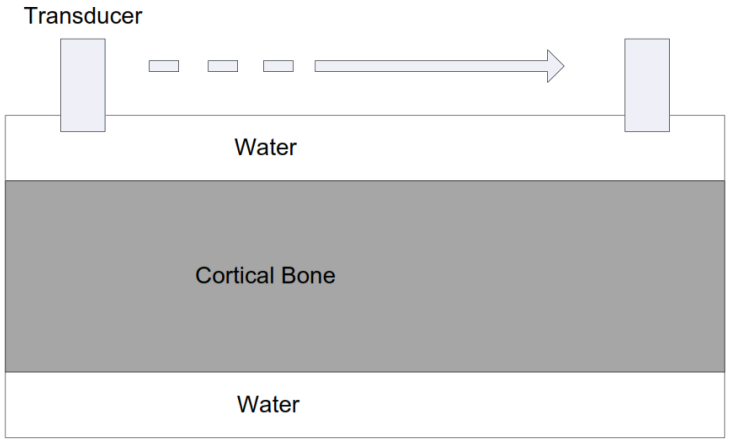

Figure 3.2: A numerical bone model for simulation.

A numerical bone model is shown in Figure 3.2. The model has 6 mm thick cortical bone with 2 mm of water above and below the bone. Here we use water to mimic the soft tissue and marrow. A pulse echo transducer is used to send and receive signals (zero-offset case), and moved along a straight line from one end of the model to the other at a spacing increment of 0.05 mm. The signal we used is a Ricker wavelet (Bording and Lines, 1997) with a central frequency of 2.25 MHz (Figure 3.3). The ultrasound velocities are 1500 m/s for marrow and 3500 m/s for cortical bone (Laugier and Haiat, 2011). The model is discretized into a 600×200 meshgrid in the *x*-*z* plane with a 0.05 mm × 0.05 mm cell size. The sampling frequency is 100 MHz, satisfying the requirement of Nyquist without introducing

aliasing. Other stable requirements of finite difference algorithms mentioned in Chapter 2 are also satisfied.

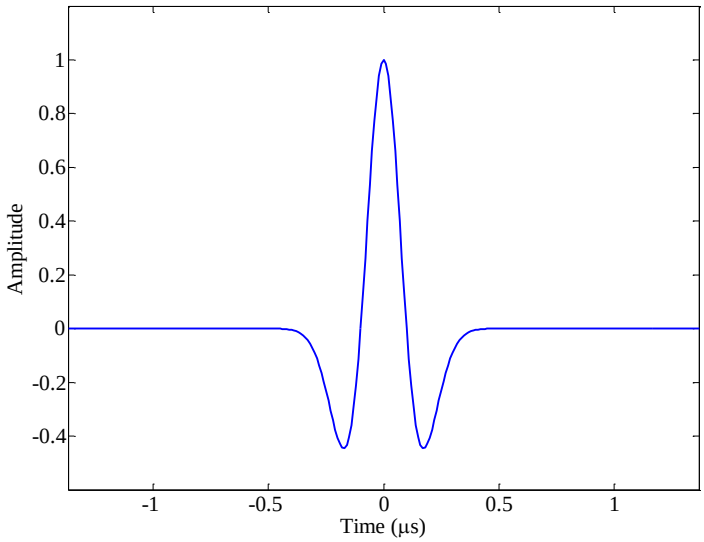

Figure 3.3: A 2.25 MHz Ricker wavelet.

3.2 Estimation of cortical bone thickness

3.2.1 Forward modeling in numerical simulation

For forward modeling, we numerically compute the signals. In our case, a finite difference approach is used to compute the observed signals via equation 2.27.

Since the finite difference approach simulates full wavefields, the waves travel in all directions along with the wave fronts. The recorded signals will include the signals reflected from the interfaces and signals reflected from a background velocity profile. If we denote the recorded signals as U , reflected signals as U_r, and background signals as U_b, then the reflected signal will be U_r =

U - U_b. The velocity model for computing U is shown in Figure 3.4(a), which is composed of a layer of cortical bone bounded above by soft tissue and below by marrow. For the background velocity, we use the model in Figure 3.4(b), a smoothed version of the velocity in (a), to compute the background signal U_b. Then the reflected signal will be the subtraction of the two. We use a disk filter with radius of 1 mm and a moving average of 11 points to smooth the original velocity model (Figure 3.4a), creating a smoothed velocity model with a blurred area of about 2 mm wide (Figure 3.4b).

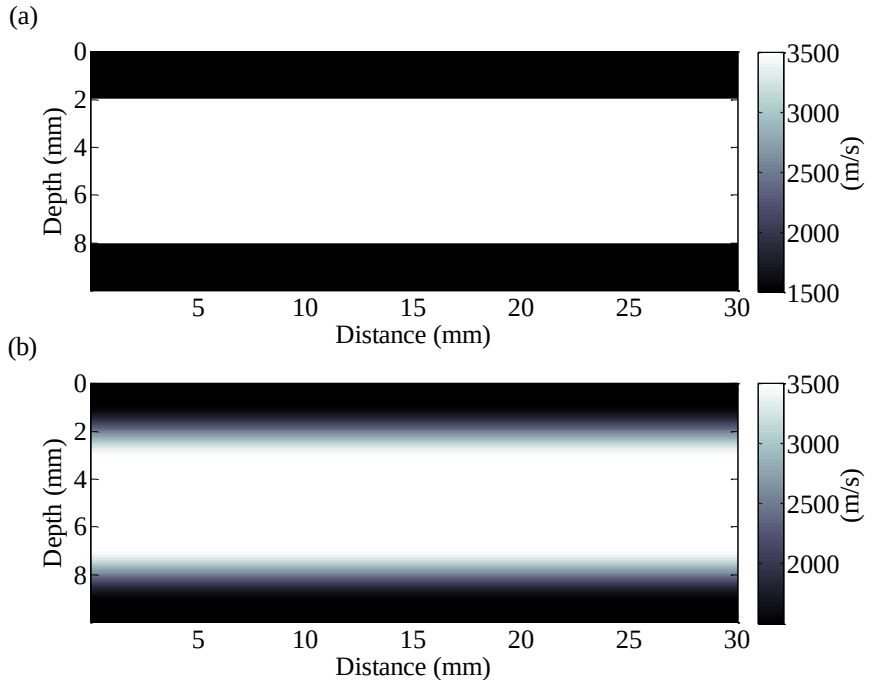

Figure 3.4: Velocity models for forward modeling: (a) a true velocity model; (b) a smoothed version of (a) obtained by a disk filter and moving average.

The simulated data is shown in Figure 3.5. Each record has 1500 data points with time increment of 0.01 μs. It is clear to see from the figure that the main

reflections are at 2.5 μs and 6 μs. The first reflection is from the soft tissue/cortex interface and the second one is from the lower marrow/cortex interface. The first reflection is much stronger than the latter one for each record as expected due to attenuation by distance travelled. Also, we see some artifacts in the computed signals, which are caused by the imperfect absorbing boundary conditions we used.

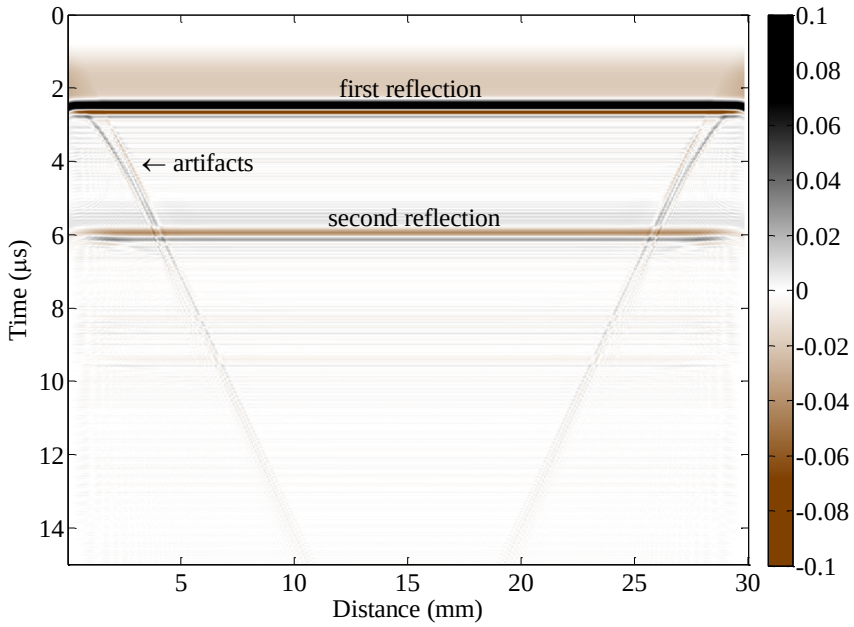

Figure 3.5: The simulated wavefields U_r using velocity models shown in Figure 3.4. The first reflection is from the cortex/soft tissue interface and the second one is from the lower marrow/cortex interface.

The data thus simulated by this simple flat-layer model will be used to test the migration algorithms. One might argue that the position of the reflections can be calculated if we know the velocity, i.e., by multiplying the velocity of the

medium by half of the corresponding traveling times. However, for a complex velocity structure with non-parallel interfaces, simple calculation will fail and depth migration is able to focus the scattered wavefields to their sources, which are the locations of the reflectors.

3.2.2 Imaging and thickness estimation

The first model is intended to test the ability of the methods to measure the intact cortical bone thickness. For the migration part, since we assume that the true velocity model is unknown, the best velocity model we can use is based on the calculation of travel distance from velocity and travel time, which is provided in the signal recorded. Also, we will smooth the reflecting interfaces to eliminate the calculation error. As a result, the smoothed velocity shown in Figure 3.4(b) is used as the migration velocity model in the numerical simulation, which is the best guess about the velocity we can get without any knowledge of the true velocity distribution.

The migrated depth images are shown in Figure 3.6. We use both methods of RTM (Figure 3.6a) and SSFM (Figure 3.6b). The images of the reflecting interface are shown by dark black and dark brown colors, where black stands for positive values and brown for negative values. Comparing with the velocity model in Figure 3.4(a), although some migration artifacts can be seen on the corners of the images, both methods reconstruct the images of the reflecting interfaces very well, showing the correct positions. In addition, the amplitude also

provides information about impedance contrast. For instance, the black amplitude is positive; showing the layer below the interface has a larger velocity than the layer above. The brown amplitude, on the other hand, shows exactly the opposite, i.e., the layer below the interface has a smaller velocity than the layer above. The relative velocity contrast information derived from the image is consistent with the original velocity model.

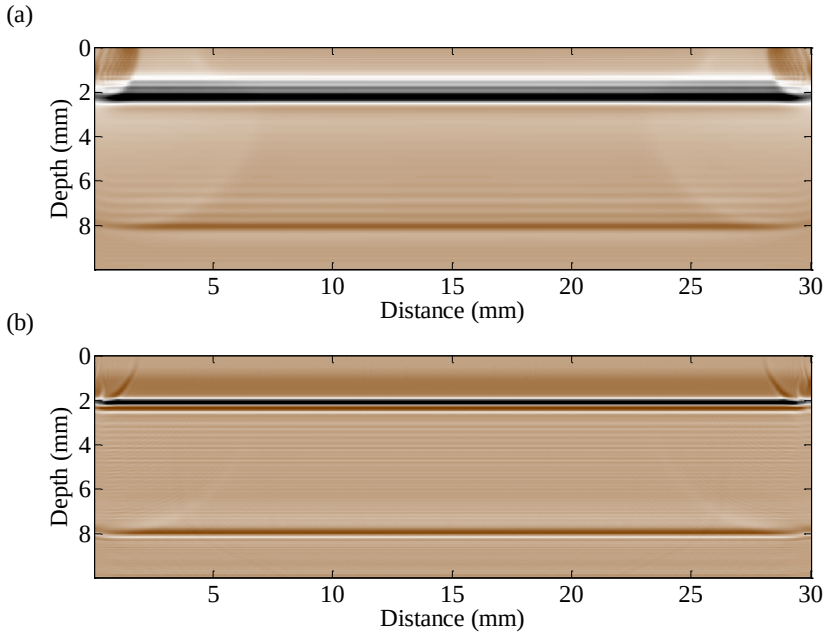

Figure 3.6: Depth migration of intact bone model: (a) results by RTM and (b) results by SSFM.

To estimate the cortical thickness, we plot the migrated depth series at a distance of 15 mm (Figure 3.7b) and compare it with the true velocity model (Figure 3.7a). The black curve in Figure 3.7(a) is the true velocity model where the sharp edges represent the positions of the interface. In Figure 3.7(b) the curves

of the migrated image are self normalized, so that the relative amplitudes fall within ±1. According to the exploding reflector model, the migrated images are the wavefields at the reflector position and the amplitude is proportional to the reflection coefficient of the reflector. So the self normalized curves show the relative reflectivity at the reflectors. The red dashed and blue dotted curves are migrated depth series from the RTM and SSFM respectively. If we pick the peak and trough as the positions of the first and second cortical interfaces, the error of the thickness estimate will be less than 0.5 mm. The reconstructed edges of the SSFM looks sharper than those of the RTM. But the latter one is smoother in the region between two interfaces, while the former has a lot of bumps in between. The second interface will have smaller amplitude than the first one because of the energy loss due to longer distances travelled and further partitioning of energy at the second interface. The change of polarity is obvious in the image, especially for the RTM case, showing the changes in polarity of velocity contrast.

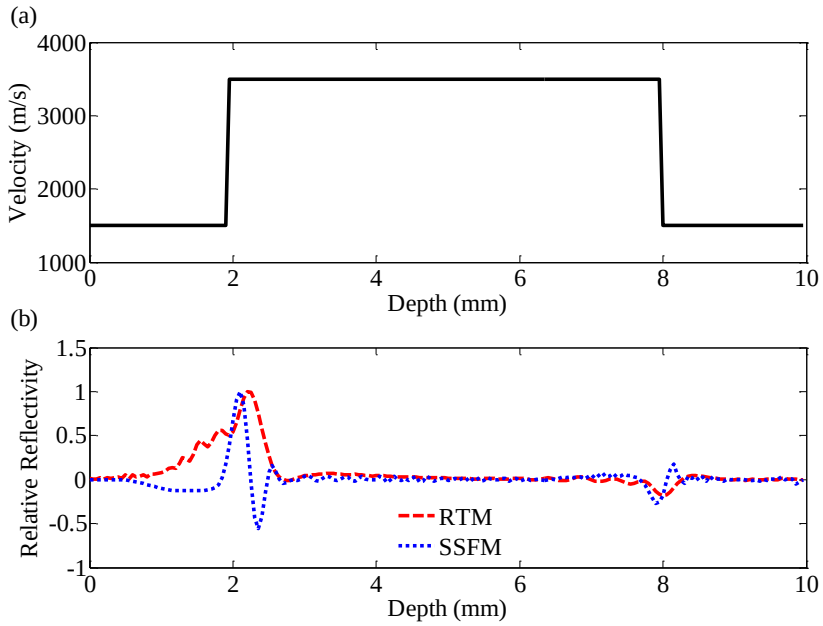

Figure 3.7: Estimation of cortical thickness and comparison of the migrated depth series with the true velocity model: (a) the true velocity model; (b) the relative reflectivity in the migrated results.

3.3 Detection of small fractures

3.3.1 Imaging a 45 degree dip fracture

We first establish a fracture model with a small fracture at 45 degree dip angle from the horizontal in the cortical bone. The apparent width (measured across the fracture horizontally at fixed depth) of the fracture is around 0.2 mm, as shown in Figure 3.8. The velocity in the fracture is 1500 m/s. Considering the first few weeks of bone healing when the fracture is filled with soft callus and tissue fluid, this assumption is valid.

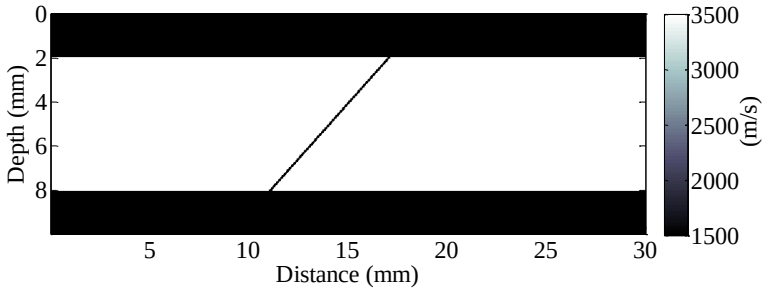

Figure 3.8: A velocity model for a fractured cortical bone.

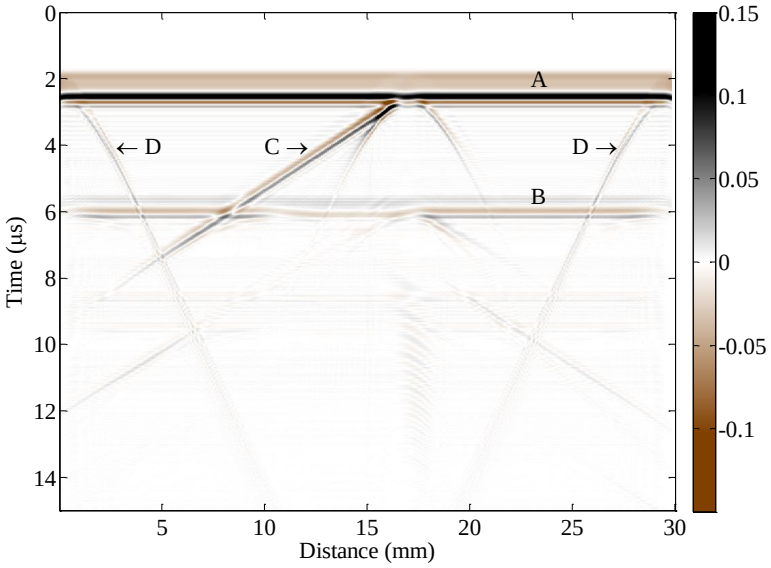

Figure 3.9: The simulated signals from a 0.2 mm fracture model with 45 degree dip angle. A and B are reflections from the top and bottom interfaces; C is the reflection from the fracture; D indicates the computational artifacts.

The simulated data is shown in Figure 3.9. Although some boundary artifacts and multiples exist in the image, we can still see the strong reflections from the different interfaces: the skin-cortical interface, cortical-marrow interface, and the fracture. There should be two reflections associated with the interfaces of the

fracture; however, since the fracture is too small, the two reflections cannot be resolved and appear as a single reflection.

From Figure 3.9, one can predict that there is a fracture in the bone between 5 mm to 17 mm. But is this inference correct? Besides, we cannot get any information about the depth of the fracture and the dip angle. So in order to collect more details about the geometric information of the fractured bone, depth migration is needed here.

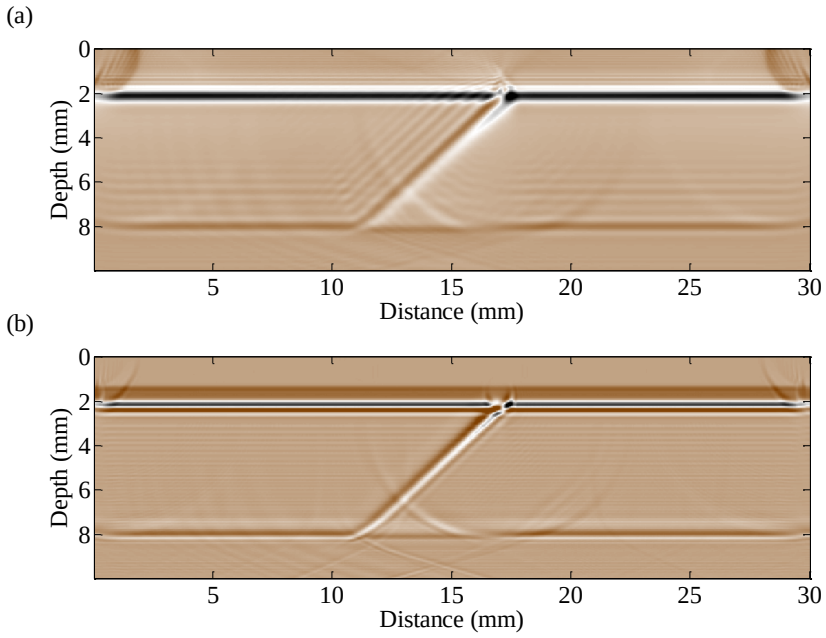

Figure 3.10: Depth migration of the 45 degree dip and 0.2 mm fracture model: (a) results by RTM; (b) results by SSFM.

For the migration, since the fracture position and dip angle are unknown, I use the velocity model shown in Figure 3.4b as my best guess. The model is a smoothed velocity model without any information about the fracture. As before,

the RTM and SSFM methods are applied. The results are shown in Figure 3.10. Compared with the original model in Figure 3.8, the fracture position is exactly reconstructed. There is amplification of the fracture size, which is due to the small dimension of the fracture and wave dispersion as the energy decreases. However, the locations as well as the dip angle are all correctly imaged. To detect small size fractures, migration methods are superior to the axial transmission ultrasound, which is only effective when the fracture size is much larger, around 20 mm (Lowet and Van der Perre, 1996).

3.3.2 Imaging 70-degree dip and 80-degree dip fractures

We change the dip angle to be 70 degrees and 80 degrees respectively with respect to the horizontal direction, while maintaining the fracture size to be 0.2 mm, same as in the previous case. The calculated signals are shown in Figure 3.11. Compared with Figure 3.9, as the dip angle becomes more vertical, the recorded echoes get weaker. Most energy reaching the fracture is reflected at close to the horizontal direction according to Snell's law, which means the receiver at the same position as the source records little reflected energy. In fact, from Figure 3.11, we can see that the reflected signal is so weak that its strength is even smaller than the amplitude of artifacts in the numerical model. So it is difficult to predict if there is a fracture in the bone based on the simulated data. Also, as the dip angle becomes larger, the multiples and some artifacts get stronger, making it

hard to distinguish the reflected signals due to the fracture from these unwanted effects.

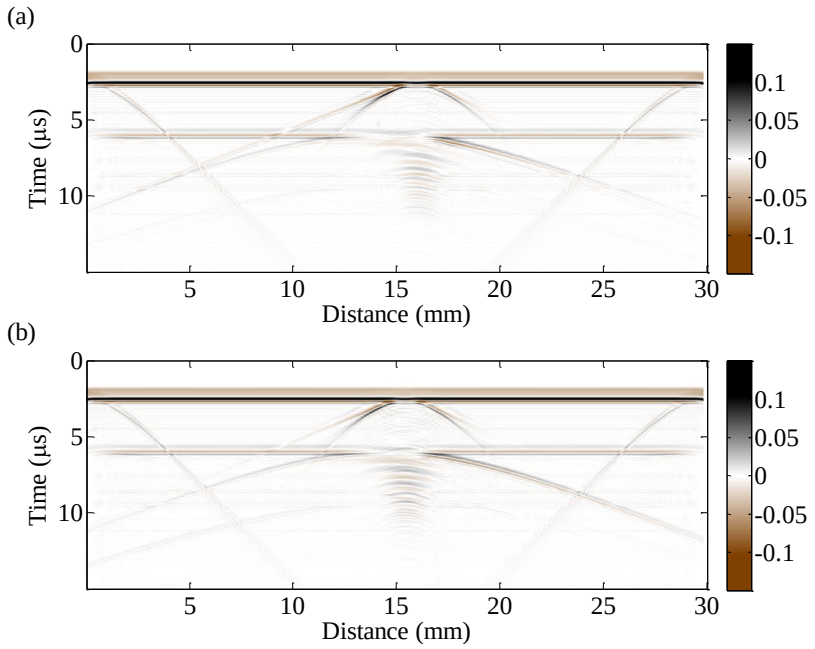

Figure 3.11: The simulated wavefields when the fracture dip angles are (a) 70 degrees and (b) 80 degrees respectively.

In the migration process, we again use the smoothed velocity model shown in Figure 3.4(b), which does not take into account the presence of the fracture. Migrated results are shown in Figure 3.12. In the 70-degree dip case (Figure 3.12(a) and (b)), both migration methods reconstruct the fracture at its correct position and dip angle. However, when the dip angle changes to 80 degrees, we can see that the reconstructed images are not as clear as before. The area of the fracture is blurred and the wavefields are not completely refocused, creating many

ringing artifacts. Zero-offset migration methods are not appropriate to image large dip angles, especially when the fracture is almost vertical (>80 degrees).

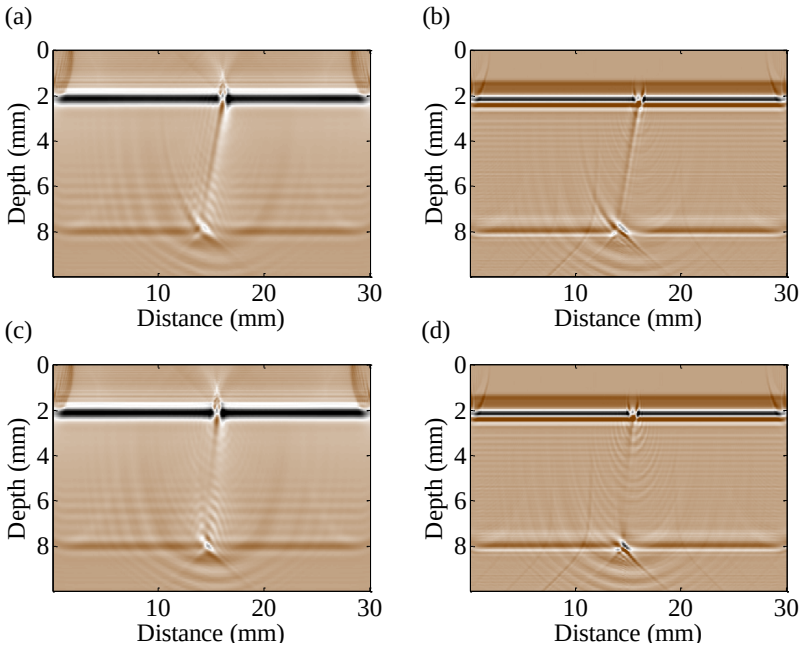

Figure 3.12: The migrated results: (a) 70-degree dip using RTM, (b) 70-degree dip using SSFM, (c) 80-degree dip using RTM, and (d) 80-degree dip using SSFM.

3.3.3 Signals with noise

The stability of the method is tested by adding noise to the simulated signals. We use the 45 degree dip angle fracture model. Gaussian noise is generated and added to the signals, with a mean of zero and standard deviation same as the signal (peak signal to noise ratio about 2). Figure 3.13 shows the noise contaminated signals. Compared with Figure 3.9, the added noise makes the signals a little fuzzy. Not only the small signals are immersed in the noise, but also large reflected signals look less sharp as before. Fortunately, although faint, the weak signals reflected

from the fracture and the lower layer of the cortical can still be distinguished from the noisy background. So from the simulated section, we can predict that a fracture exists in the cortical bone model, although we cannot tell the exact position of the crack.

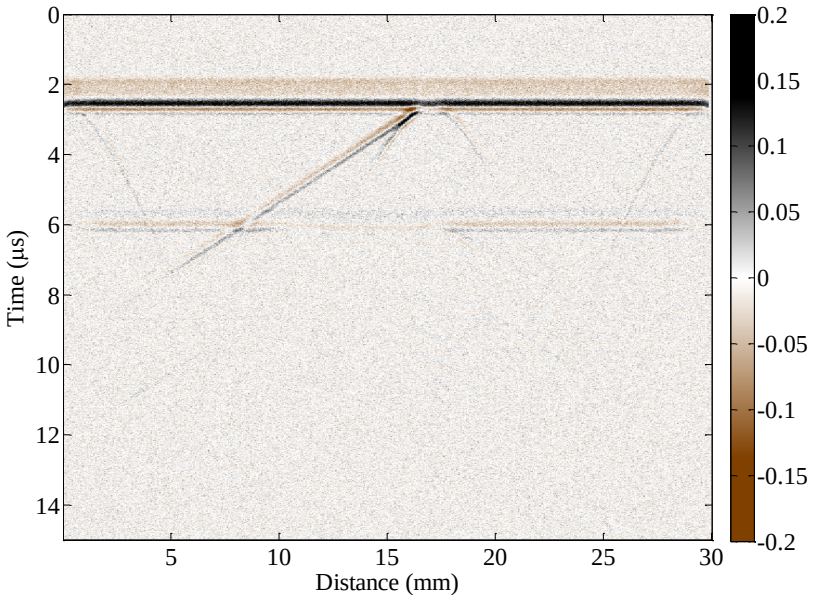

Figure 3.13: The simulated signals with Gaussian noise.

Using the smoothed velocity model (Figure 3.4b) as the initial guess, the migrated image by the RTM and SSFM methods are shown in Figure 3.14. Compared with the noise free results (Figure 3.10), we see that the reconstructed image can still present the structure of the original velocity model (in Figure 3.8) correctly. However, the images here seem noisier and the reconstructed lower layer is not as sharp as before. On the other hand, those noises also eliminate the

migration artifacts as shown in Figure 3.10, emphasizing the major reflection interfaces.

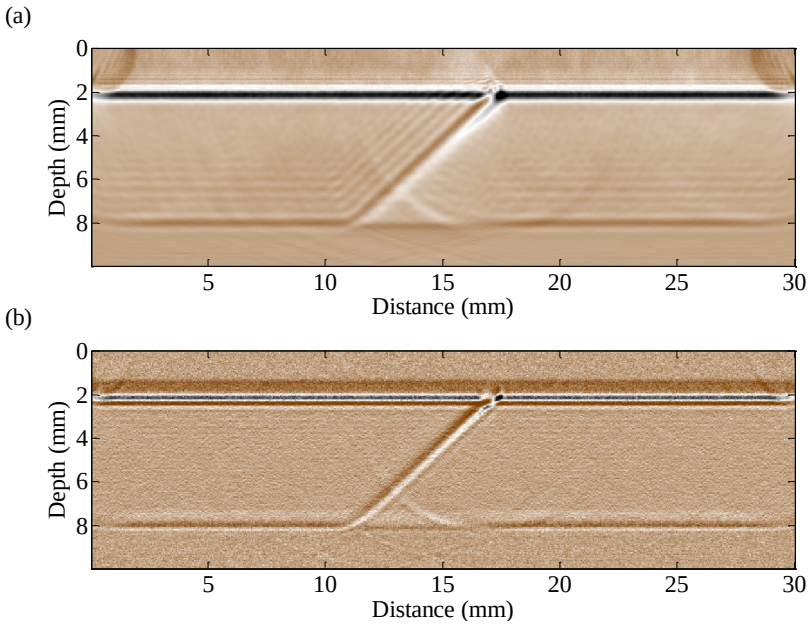

Figure 3.14: Depth migration of 45-degree dip angle and 0.2 mm fracture model (Figure 3.8) with Gaussian noise added (Figure 3.13): (a) results by RTM; (b) results by SSFM.

Both migration methods are quite stable in the presence of noise. Although adding noise to the signals can make the reconstructed image a little blurred, some migration artifacts are also eliminated to highlight the reconstructed interfaces in the noisy background.

3.4 Iterative imaging when fracture is large

The fractures discussed so far are small size fractures, with width not more than 0.2 mm, which we can call mini-fractures. When the fracture in the bone becomes larger, it is uncertain if the migration method works.

For the same fracture with dip angle of 45 degrees, we enlarge the width of the crack to 0.5 mm, 1 mm, and 2 mm to see how good the migration results will be. The velocity models are shown in Figure 3.15. As before, the ultrasound velocity is 3500 m/s for cortical bone, and 1500 m/s for soft tissue, marrow, and the fracture tissue.

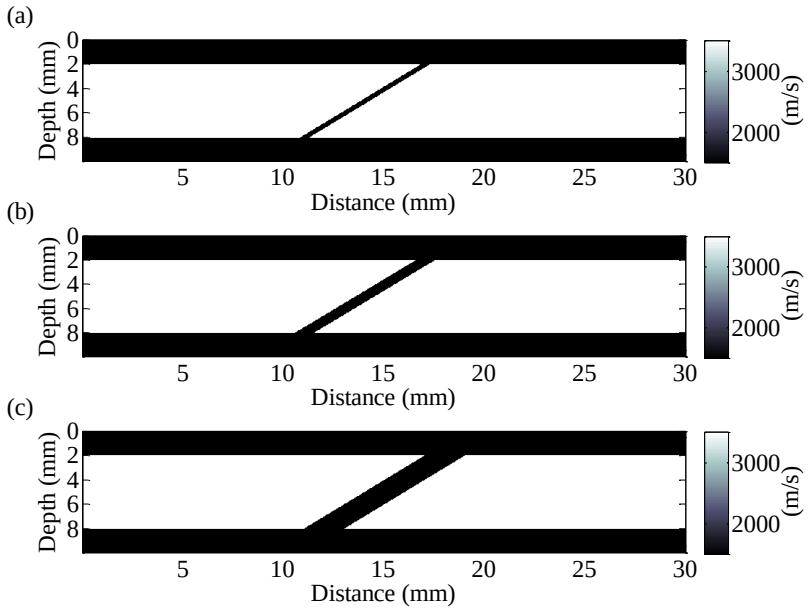

Figure 3.15: The velocity models for different fracture sizes: (a) 0.5 mm, (b) 1 mm, and (c) 2 mm. These are the apparent widths measured horizontally across the fracture at fixed depth.

The simulated signals are shown in Figure 3.16. As the size of the fracture increases, the signals reflected from the cortical bone-soft tissue interface are almost the same. For the echoes from the left and right boundaries of the crack, we can see that they fall into two separate reflections as the size of the fracture increases. The separation becomes evident in Figure 3.16b, when the fracture size

increases to 1 mm. However, due to the velocity differences between the cortical bone and fracture tissue, the reflected signals from the cortical bone-marrow interface beneath the fracture area are delayed and this effect becomes much more obvious when the fracture size is larger, as shown in Figure 3.16c.

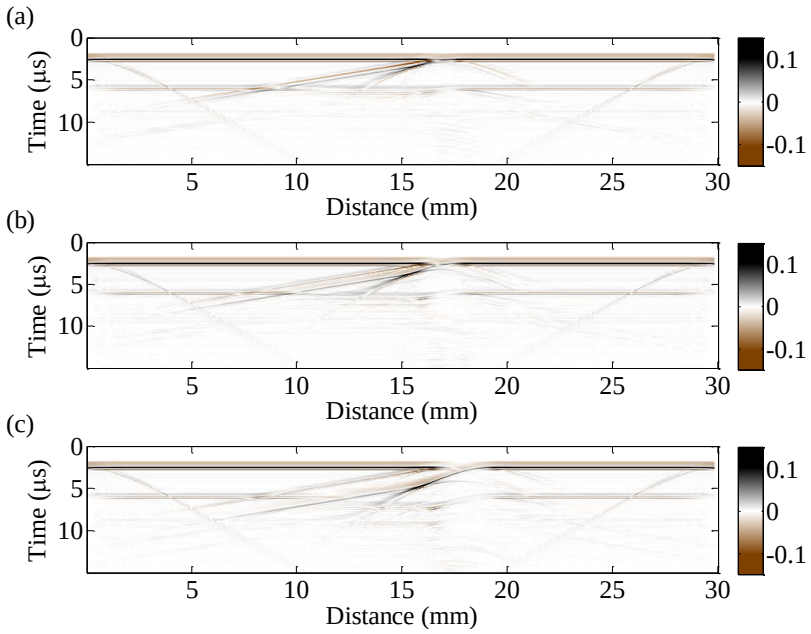

Figure 3.16: The simulated wavefields: (a) 0.5 mm fracture, (b) 1 mm fracture, and (c) 2 mm fracture.

The presence of the fracture adds complexity to the echograms as compared to the simple one layer cortical bone model. We find that as the fracture size increases from 1 mm to 2 mm, the reflected signals become much more complicated, as shown in Figure 3.16(b) and (c). Simple calculations using velocity multiplication with travel time will be hard to estimate the crack

thickness. Fortunately, migration methods give us an alternative and relatively precise way to do the model reconstruction.

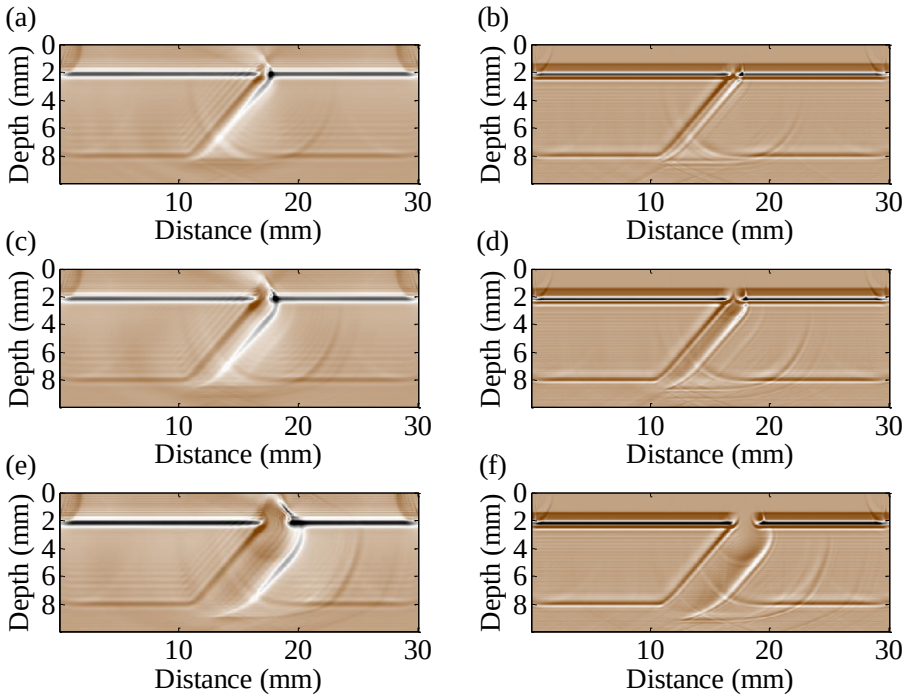

Figure 3.17: The reconstructed fracture images by RTM (a, c, and e) and SSFM methods (b, d, and f). The fracture sizes are 0.5 mm (a, b), 1 mm (c, d), and 2 mm (e, f).

Using the input velocity model shown in Figure 3.4(b), the reconstructed models are presented in Figure 3.17. We can clearly see the fracture in each case. Compared with the original models in Figure 3.15, however, there is an amplification effect in the reconstructed images, which shows that the reconstructed fractures widths are larger than their original model widths.

Taking a closer look at the interfaces bounding the fracture, the left interface is always correctly imaged for both the dip angle and the position. The right

interface, however, is reconstructed to a position slightly lower than the true position. As the fracture size becomes larger, the right interface becomes much further from its correct location. That is to say, the sizes of the imaged fracture are bigger than the model size. This amplification effect is due to the velocity model we used in the migration. Because we do not know any prior information about the fracture in the cortical bone, the first guess of the velocity model will be the simplest one, as shown in Figure 3.4(b). The initial model does not consider the fracture and assigns 3500 m/s for the whole cortex layer. Therefore in the fracture area, the assumed velocity is much larger than true velocity, 1500 m/s. As a result, the reflected signals that travel in the fracture part will be migrated to a further reflecting position, which lowers the position of the interface and make the fractures look larger.

In order to better image the bigger fracture and reduce the amplification effect of the migration using the simple velocity model without information about the fracture, an iterative migration method should be used. The iterative approach will take the results from the first migration pass and rebuild a more precise velocity model as the input for the second-pass migration. As we have analyzed, the soft tissue-cortical bone interface as well as the left interface between cortical bone and fracture tissue are both correctly imaged. We can use these two interfaces to build a more precise velocity model. Figure 3.18 shows the process

to reconstruct a better velocity model from the first-pass migrated images. Figure 3.18(a) and (c) are just the same migration results as Figure 3.17(d) and (f).

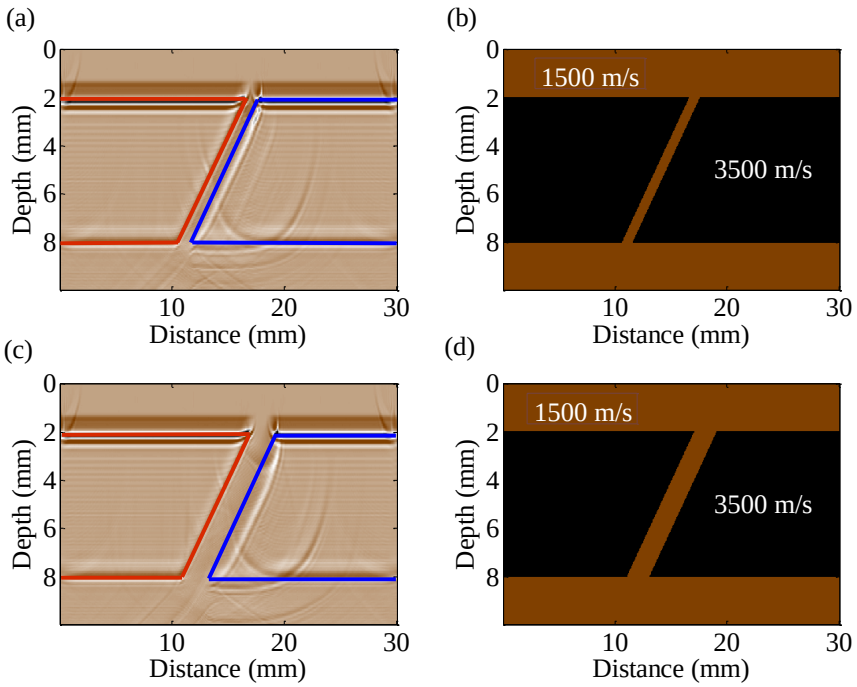

Figure 3.18: Rebuilding a better velocity model from the first-pass migrated images: (a) same as Figure 3.17(c) with the outlines of the interface boundaries; (b) the corresponding new velocity model of (a); (c) same as Figure 3.17(d) with the outlines of the interface boundaries; (d) the corresponding new velocity model of (c). See text for the description of the colored lines.

The rebuilding procedure of the velocity model is as follows. First, from the migrated results in Figure 3.18(a) and (c), we find the correctly imaged interfaces. It is inferred that the soft tissue-cortical bone interface, left cortical bone-fracture interface and part of the cortical bone-marrow interface are correctly located in the migrated image. We highlight these interfaces with red lines, as shown in the

figures. To locate the right fracture-cortical bone interface, we use the discontinuity of the upper soft tissue-cortex interface as guidance. We draw the parallel line to represent the assumed location of the interface, as is shown by the blue lines in the figure. As a result, we use the interfaces contoured by the red and blue lines to rebuild a better velocity model, as shown in Figure 3.18(b) and (d). Another migration procedure is then applied based on these new velocity models.

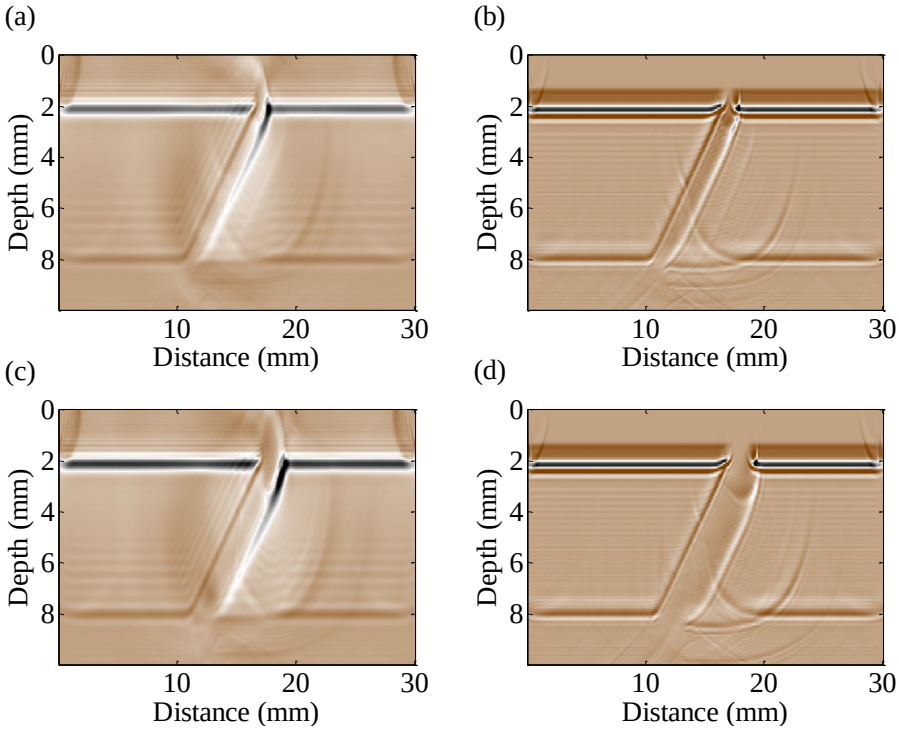

Figure 3.19: The second-pass migrated images by RTM (a and c).and SSFM (b and d) of the 1 mm fracture (a, b) and 2 mm fracture (c, d).

The second-pass migration results for the 1 mm and 2 mm fractures are shown in Figure 3.l9. For both fracture sizes, compared with Figure 3.17(c), (d), (e), and (f), the second-pass migrated results are better, with the fractures more

precisely imaged, especially the right fracture-cortical bone interfaces. When the fracture size is small, the migration result by both reverse time and split step migration methods are almost the same. However, when the fracture size is 2 mm, we notice that the RTM method tends to achieve a better result than SSFM, as compared between Figure 3.19(c) and (d). This is because in the SSFM, an averaged velocity will be used in the migration process, whereas in RTM, there is no such approximation.

After a simple iterative migration, the migrated results will get better compared to the original model. Here we only do the migration two times and actually more iteration steps can be preformed if needed. In a general case, the SSFM method will need more iterations than the RTM method to achieve a desired resolution for a large-size fracture case.

3.5 Monitoring of the fracture healing process

The fracture healing process, as described in Chapter 1, involves complex biological and chemical reactions. In this section, we simulate the healing process by changing the ultrasound velocity of the fracture zone, from the tissue velocity at the beginning of the healing process to the cortical velocity at the end of the process. The basic idea behind this assumption is simple. As the fracture heals, the material in the fracture will gradually change from blood and tissue fluid (Phillips, 2005; Schindeler *et al.*, 2008) to cortical bone as a result of callus mineralization and ossification.

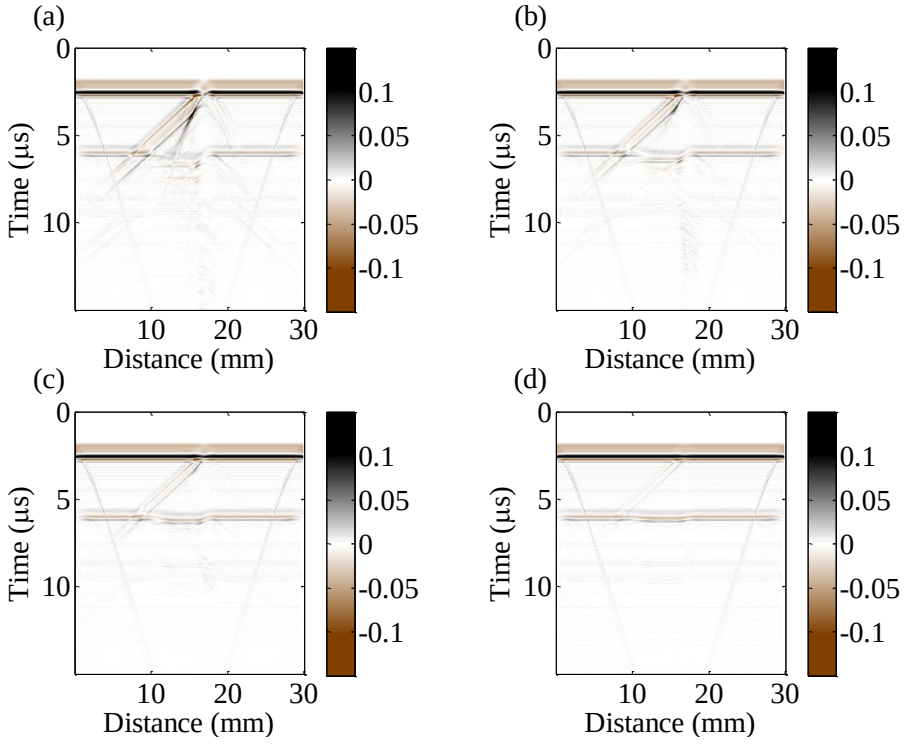

Figure 3.20: The simulated signals at various stages of the healing process. Velocities at the fracture are (a) 1500 m/s, (b) 2000 m/s, (c) 2500 m/s, and (d) 3000 m/s, respectively.

To simulate the healing of a 1 mm 45 degree dip fracture, we change the ultrasound velocity of the fracture tissue from 1500 m/s to 2000, 2500 and 3000 m/s, respectively while holding all parameters the same. The simulated signals for each case are shown in Figure 3.20. We see that as the velocity in the fracture increases, the reflected signals from the left and right interface are less obvious. This is consistent with equation 3.2, which tells us that as the velocity difference decreases, the reflection coefficient also decreases. In fact, for the model where ultrasound velocity in the fracture equals 3000 m/s, the signal strength of

reflections around the fracture area are extremely weak and even smaller than that of the multiple reflections (Figure 3.20d).

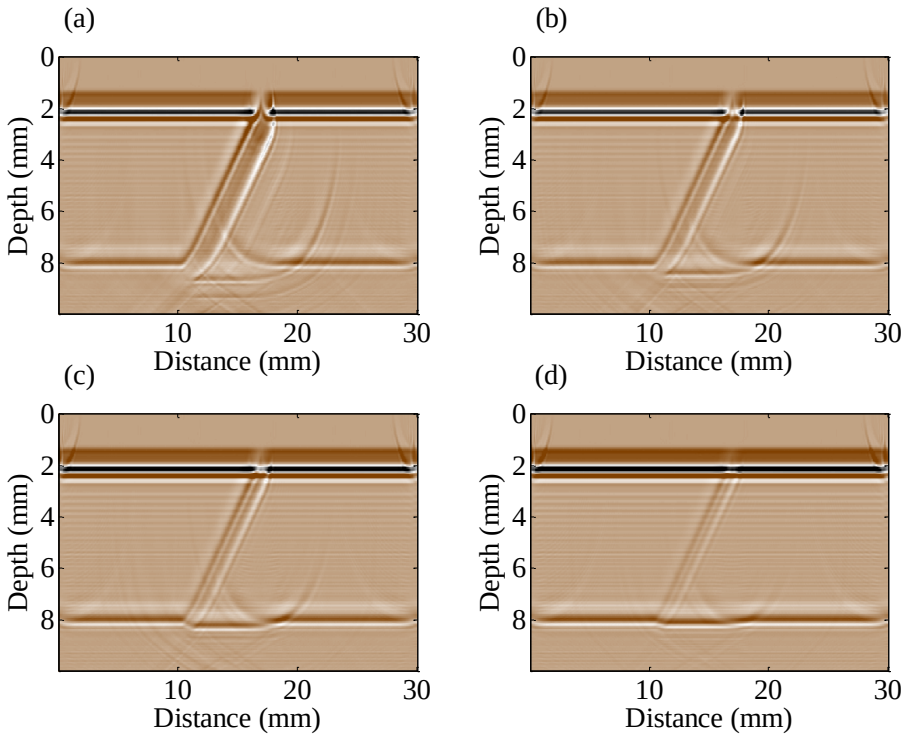

Figure 3.21: The reconstructed images at various stages of the healing process using SSFM. Velocities at the fracture are (a) 1500 m/s, (b) 2000 m/s, (c) 2500 m/s, and (d) 3000 m/s, respectively.

Using a general velocity model without a fracture (Figure 3.4b), we reconstruct the four images using the simulated data shown in Figure 3.20. Both migration methods are used, and here we present only the results of SSFM in Figure 3.21. We can see that when the fracture velocity increases, the shape of the reconstructed image changes significantly. The width of fracture decreases, which eliminates the amplification effect in fracture size shown in Figure 3.21(a). Also,

the migration artifacts will become smaller at larger fracture velocities. Although the signals are small in Figure 3.20(d), the migrated image in Figure 3.21(d) is still clear enough to see the healing fracture. Using the migrated images, we can tell the healing status as fracture heals. In a true amplitude case, it is possible to calculate the reflection coefficients from the amplitude, and use the reflection coefficients to calculate the true velocity of fracture, which may be used as a mechanical property to determine the fracture healing process.

3.6 Summary

In this chapter, numerical simulations were performed to demonstrate the possibility of using migration methods to detect bone structures. First, a theoretical model of an intact bone was established, and we used migration to estimate the cortical bone thickness, a parameter very useful in osteoporosis diagnosis. Then some fracture models were constructed for various fracture dip angles and fracture sizes. Using these models, simulated data sets were generated to validate the imaging methods and their robustness in the presence of Gaussian noise. The method worked well if the fracture dip angle was less than 80 degrees from the horizontal axis. It could resolve the small fractures, such as 0.2 mm, and was quite robust in the presence of noise. For larger fractures, an iterative migration strategy should be used to improve the imaging accuracy. Lastly, we fabricated a model to monitor the fracture healing process, by increasing the

ultrasound velocity of the fracture tissue as it heals. All the computing results seemed very encouraging.

Both zero-offset reverse time migration and split step Fourier migration were used in reconstructing the images. The results of both migration methods seemed quite similar for all the cases, except the one with larger-size fracture, but the difference was small. Generally speaking, the RTM method provides better results than the split step method, since the latter involves an average velocity assumption in the computing. However, because the split step method works in Fourier domain to avoid time consuming space-time computation, it works much faster than RTM. For a simple model in our simulation, such as the simple 45-degree 0.2 mm fracture model, the SSFM method takes no more than 1 min, while RTM takes about 10 hours on a 4-core, 3GB-memory computer (Windows XP, Intel Core Q6600 2.40 GHz). Given that both migration methods give us similar results and the split step Fourier method has a much faster computational speed, we will apply SSFM to image real bone fractures in the next chapter.

In the migration process, the background velocity is required as one of the inputs along with the signals. This velocity is an initial guess of the velocity distribution in the bone. It does not have to contain the details in the media, such as the fracture positions or accurate velocity value in the bone. If we have the true velocity model, migration is not needed. In the case when the velocity model is unknown, the smoothed background velocity is useful in eliminating computing

errors of the false velocity assumption. However, the initial guess of the background velocity should be as accurate as possible in order to obtain the correct positions of the reflecting surfaces. For example, we can sign other velocities to the cortex part, such as 3000 m/s or 4000 m/s in the migration. In such cases, we can still achieve the migrated results showing the cortical bone and fracture interfaces. However, the cortical bone thickness will get smaller (3000 m/s) or larger (4000 m/s) than the real thickness. Fortunately, since the ultrasound travel time in cortical bone is small, the induced error in these two cases is less than 1 mm. So the migration methods are quite stable in the presence of bone velocity estimation errors.

Chapter 4. Image reconstruction of phantom and bone data

4.1 The experiment setup

In the previous chapter, all data were simulated using the finite difference approach. In this chapter, we further our research to reconstruct images of some phantom and real bone data acquired through experiments. The experimental setup is composed of the measuring system, the transducer, and the mechanical system.

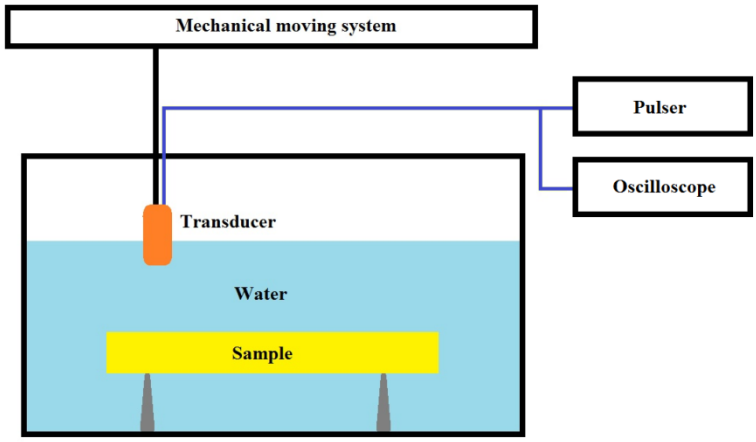

Figure 4.1: A sketch of the experimental setup.

A sketch of the experiment setup is shown in Figure 4.1. The measurement is taken in the water. The sample is placed in a water-filled tank and rests on two rubber holders. A transducer is connected to the pulser and the oscilloscope. The

mechanical system is designed to hold the transducer and be able to translate the transducer along the sample at 1 mm per step.

The measuring system is composed of an ultrasonic pulser-receiver (Panametrics® computer controlled pulser/receiver, Model 5800) and a 200 MHz oscilloscope (Lecroy® Wavesurfer, Model 422). The pulser/receiver activates the transducer to transmit a pulse and the echoes are recorded by the oscilloscope. The pulse echo mode is used. The transducer (Olympus Panametrics-NDT C323) we use is an immersion transducer, with central frequency 2.25 MHz and nominal element size 0.25 inches (6 mm). Each record is internally averaged 128 times. Also, the original data is decimated to 1/20, making the time interval increased from 1 to 20 nano-seconds.

4.2 Image reconstruction using phantom

The first sample is a Plexiglas phantom of rectangular prism. The phantom has a dimension of 22.5 cm×10 cm×2.5 cm, and is used to mimic a cortical bone fracture with a 45-degree dip crack in the middle, as shown in Figure 4.2. There are tracks on both sides of the phantom, enabling us to change the width of the fracture by sliding two sides apart. The phantom is 24.72 mm thick and the ultrasound velocity of the Plexiglas is measured to be 2667 m/s.

We move one of the two blocks of the phantom along the track and set the width of the fracture to be 2 mm (measured horizontally). Measurement starts

from about 4 cm left of the fracture to 1 cm right of it and then move backward from right to left, at 1 mm spacing interval with 102 records acquired.

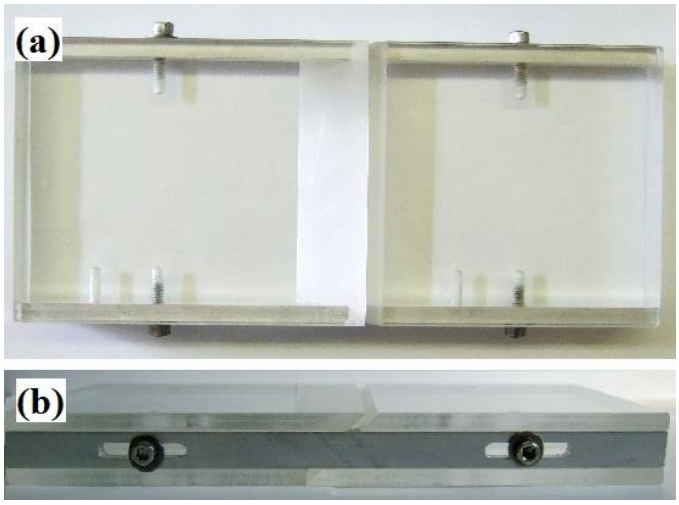

Figure 4.2: The rectangular phantom with a 45-degree dip fracture in the middle: (a) top view and (b) side view.

The recorded signals are shown in Figure 4.3. In the image, we can clearly see the first reflection from the top of the phantom, located around 25 μs. Reflections from the bottom of the phantom (around 43 μs) are also strong but broken into several sections. The reflections from the fracture are quite small signals and hardly seen. Part of the reflections from the fracture is enlarged in the subfigure. The signals at around 50 μs are the multiple reflections from the top interface and the other later signals are the reflections from the bottom of the water tank.

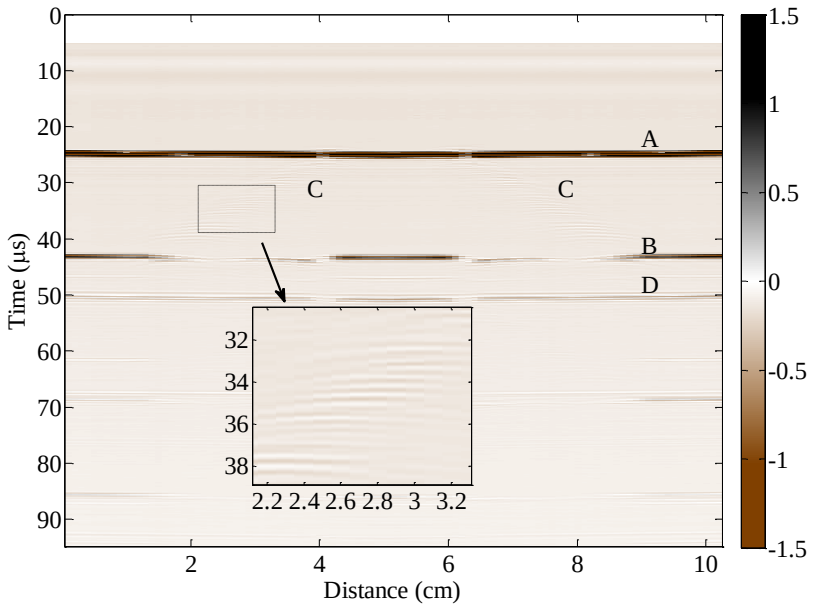

Figure 4.3: The echogram of the Plexiglas phantom. A and B are reflections from the top and bottom surfaces; C are reflected signals from the fracture, which are really weak; D is the multiple of A. The arrow illustrates an enlarged image of C.

The reflections from the fracture are quite small, compared with the numerical simulation. The underlying reason is that in the experiment, the ultrasound source is a transducer, which transmits ultrasound mainly within a finite aperture, which is quite different from the numerical simulation, where we assume the source to be a point source, sending signals radially to all directions. Considering that the directions along which the ultrasound wavefront propagates can be represented by a ray, Snell's law takes effect, and therefore the majority of the signals are reflected horizontally in the 45-degree dip case. As a result, the echoes received by the transducer at the same position as the source are very weak.

Several signal processing steps are required for the data before migration. The first step is to apply a band-pass filter (0.5/1.0/3.0/3.5 MHz) to eliminate the low frequency bias and high frequency noise. Then the reflected signals from the fracture are amplified with a simple gain by multiplying the signals between the top and bottom interfaces with a constant. The result after the gain process is shown in Figure 4.4, where we can see a big improvement of the reflections from the fracture compared with Figure 4.3. The spacing interval between records is 1 mm, which is quite large. To achieve a better resolution, an interpolation is carried out to make the spacing resolution to be 0.25 mm, one quarter of the original interval. I apply Spitz's F-X domain interpolation (Spitz, 1991). After that, normalization of amplitudes is carried out for each record in order to eliminate some artifacts in the acquisition procedure. The signals after all these signal processing steps are shown in Figure 4.5. Compared with Figure 4.4, an improvement in the signals is achieved, with better resolution and higher contrast.

Compared with the numerically simulated signals, the signals we have here are much more complicated. It seems that the fracture zone delineated by the reflected signals is much wider, which is due to the smooth reflecting surface and the ray property of the finite ultrasound beam in application. The lack of signal resolution will probably affect the migrated image resolution.

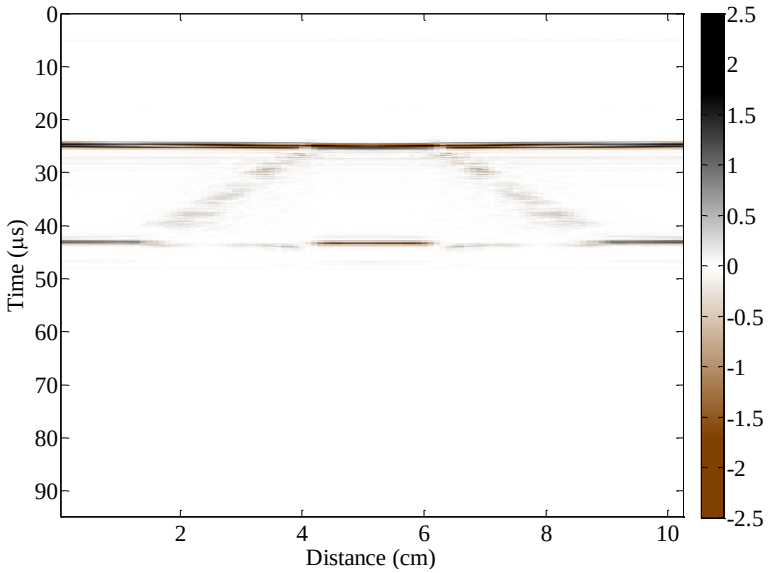

Figure 4.4: The echogram of the Plexiglas phantom after constant time gain compensation.

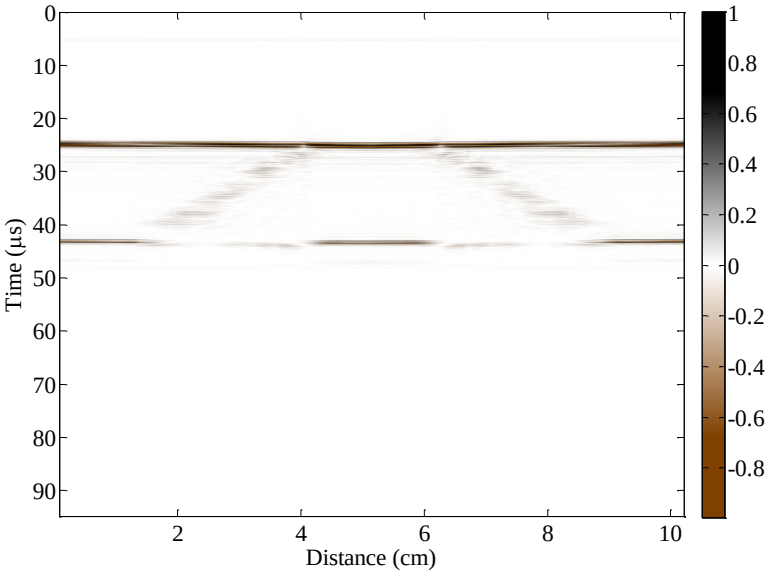

Figure 4.5: Signals after filter, gain, interpolation, and normalization.

To sum up, experiment data require some processing before the migration. The signal processing steps are summarized in Figure 4.6.

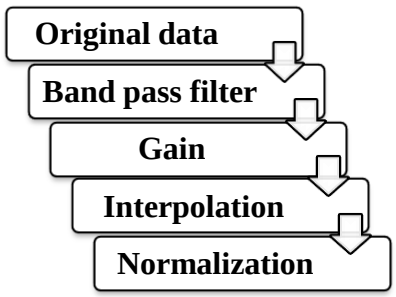

Figure 4.6: Signal processing flow chart.

For the migration process, an initial velocity model is required. As discussed in the previous section, the velocity model is established using traveled distance, which is a multiplication of ultrasound velocity in the medium with the corresponding travel time of the echoes in each record. Remember that the travel time should be divided by 2 in order to change from the two-way to the one-way travel time. A stratified layer velocity model is established through this method and then smoothed to decrease the computational error. The smoothing process is described in Section 3.2.1. The velocity model is shown in Figure 4.7.

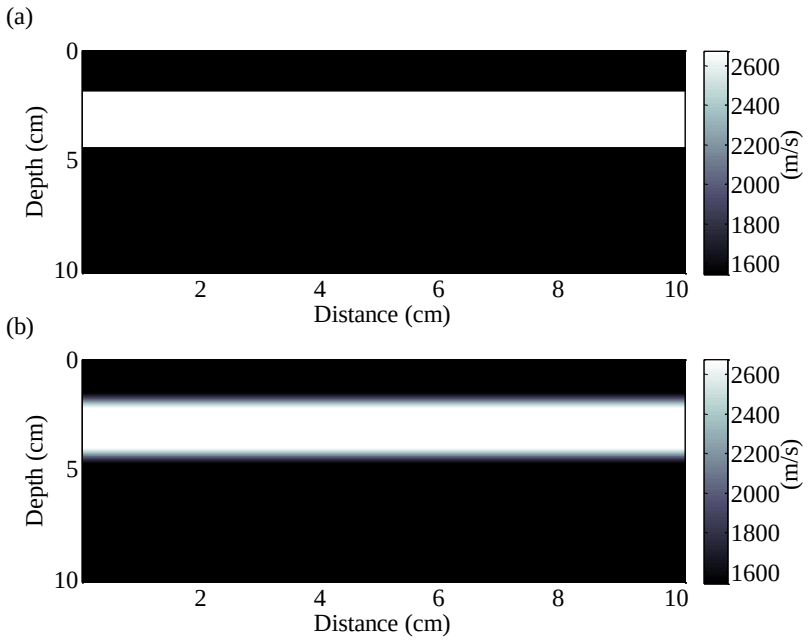

Figure 4.7: The initial velocity model for the migration process of the phantom: (a) the stratified velocity model, and (b) the smoothed version of (a).

The SSFM method is used to reconstruct the image of the phantom. As shown in Figure 4.8, the reconstructed image provides the exact depth information of the model. From the image, we obtain the thickness of the phantom, which is about 2.4 cm as shown in blue arrow with an error of 3% (compared with a measured thickness of 2.472 cm). The error is less than 0.1 mm. Also, the reconstructed fracture dip angle is 45 degrees, which is consistent with the actual dip angle. The two fracture parts are almost the same, showing that the measuring directions will not affect the image reconstruction. However, the reconstructed fracture is much wider and measured to be slightly less than 4 mm. As discussed in the previous chapter, this amplification partly comes from the rough velocity model without any prior information of the fracture. For the

experimental data, another reason is due to the character of the signals. From Figure 4.5, we see that the reflected signals are not as sharp as the simulation case. The poor resolution in the signal will also affect the reconstructed result. For the first reason, we can use an iterative migration to get a better image, but for the second one, iteration will not help. We tried a second pass migration but the result does not improve much. So the amplification here is mainly due to the poor signal resolution.

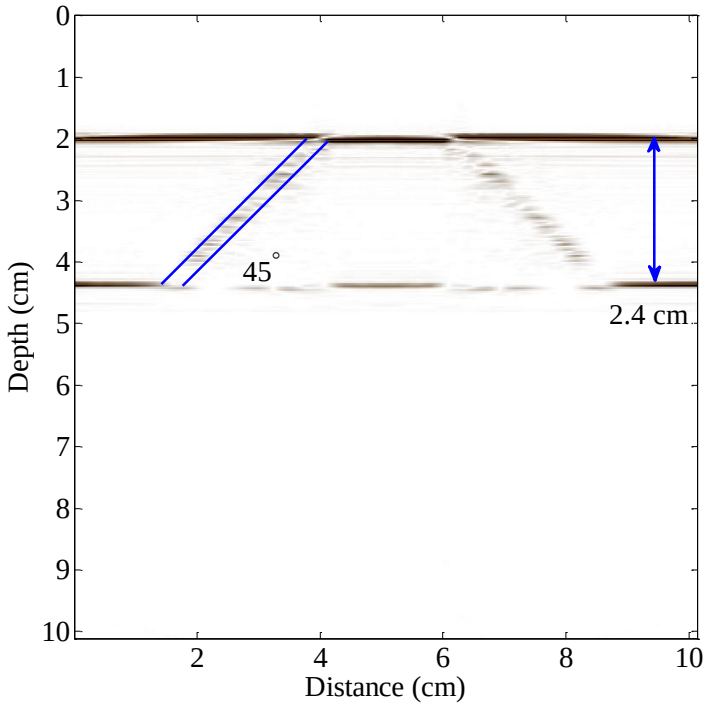

Figure 4.8: The reconstructed image of the cracked phantom.

4.3 Image reconstruction of the fractured bone plate

A long bone from deer was cut along the axial direction to obtain a cortical bone plate, which is shown in Figure 4.9. It is broken into two pieces manually. The

bone plates are supported by a copper plate and immersed in water. From the image, we can see that the fracture is irregularly shaped, which corresponds comminuted type of fractures. The blue ellipse outlines the fracture area we will focus on. The width of the fracture is around 2-5 mm. The transducers, acquisition parameters, and setup are the same as the phantom experiment.

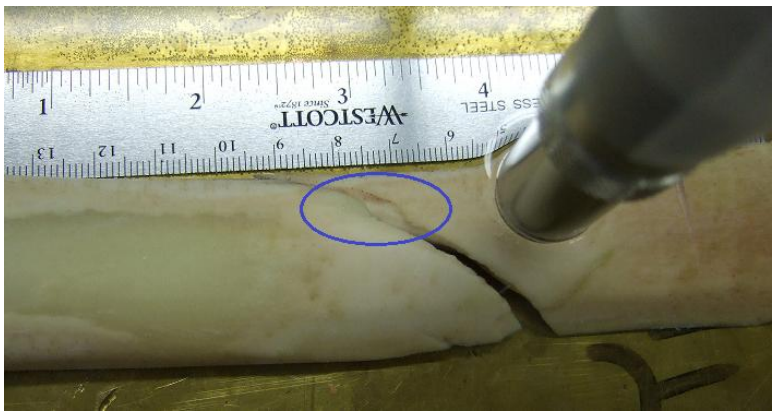

Figure 4.9: The experiment setup for the bone plate.

As the transmitter moves along a straight line, the reflected signals will provide the cross-sectional information of the bone plate. The signals recorded are shown in Figure 4.10. The reflections from the upper surface of the cortical bone are much stronger than the reflections from the lower surface. Because the cortical bone thickness is small, around 5 mm, the reflected signals from the two surfaces of bone are close to each other, with a time interval less than 5 μs. Multiple reflections can be found around 30 μs; However, they are even smaller than the reflections from the lower cortical bone surface, indicating that the reflection coefficient is small. The echogram shows a fracture in the bone plate

between 3 and 4 cm distance. However, it is difficult to obtain the shape of the fracture from a time-distance frame coordinate. Migration offers us an opportunity of changing the frame to a distance-depth view.

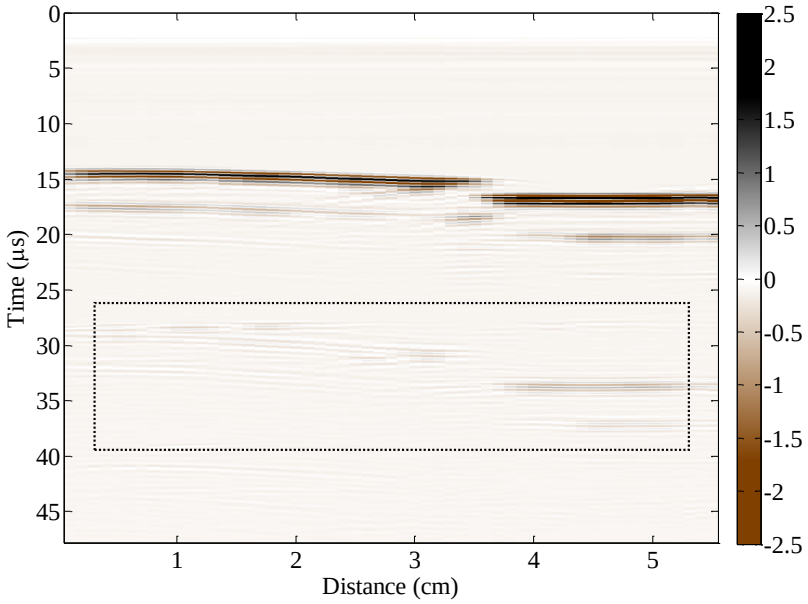

Figure 4.10: The recorded echogram for the cortical bone plate. The rectangle outlines the multiple reflections.

Before migration, the reflected signals are processed using the steps given in Figure 4.6 to enhance the signals after the first reflection in each record. The processed echogram is shown in Figure 4.11. Compared with the original signals in Figure 4.10, we can see an enhancement of the signals from the lower surface of the bone. Also, some details emerge in the processed signals, like the small reflections between the two surfaces, circled in blue in the figure. There are some side effects of the signal processing, since the signal enhancement will inevitably amplify noise as well, especially in case when the reflected signals are very small.

Therefore, for the noisy data, the original signals should be consulted to determine the fracture shapes.

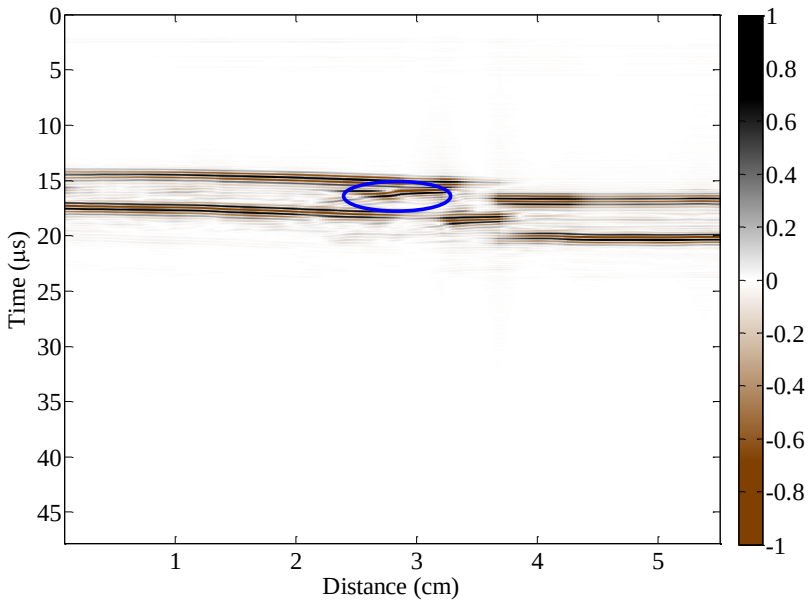

Figure 4.11: The processed echogram for the bone plate.

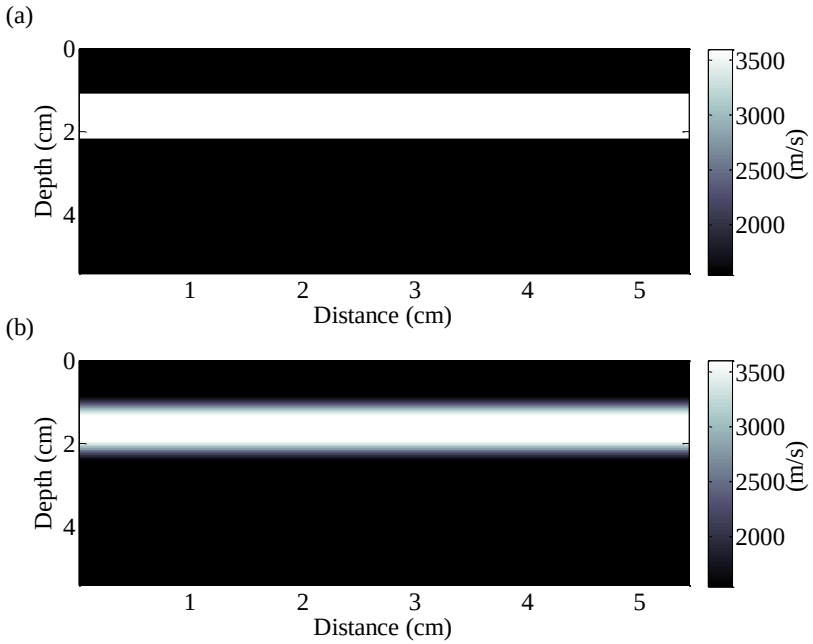

Figure 4.12: The velocity model of the fractured bone plate used for migration: (a) the original stratified velocity model and (b) a smoothed version of (a).

The velocity model (Figure 4.12) for the migration is established based on the reflected signals. The reflections are timed with the velocity of water and cortical bone being 1500 m/s and 3600 m/s, respectively. The velocity model does not include a crack. Using the SSFM method, the reconstructed depth-offset image is shown in Figure 4.13. We use blue dots to emphasize the different reflecting interfaces in the image. For experimental data, the reconstructed depth image gives us information about the location and shapes of the fracture. From the image, we measure the thickness of the bone plate to be around 5 mm and the shape of the fracture can also be detected. From the previous chapter, the numerical experiments demonstrated that for the zero-offset measurements, the imaging

technique fails to image vertical or near vertical reflecting interfaces. It is also confirmed in the experimental cases that the vertical fracture cannot be reconstructed properly. As a result, the fracture interface is partly reconstructed. That is, the vertical fracture part becomes invisible under this zero-offset migration method. Comparing with the fracture shape in the subfigures (a) and (b), we can find some similarity in the reconstructed image with the real bone plate. From the top to the bottom of the plate, the fracture has a vertical break, an oblique surface and another vertical break.

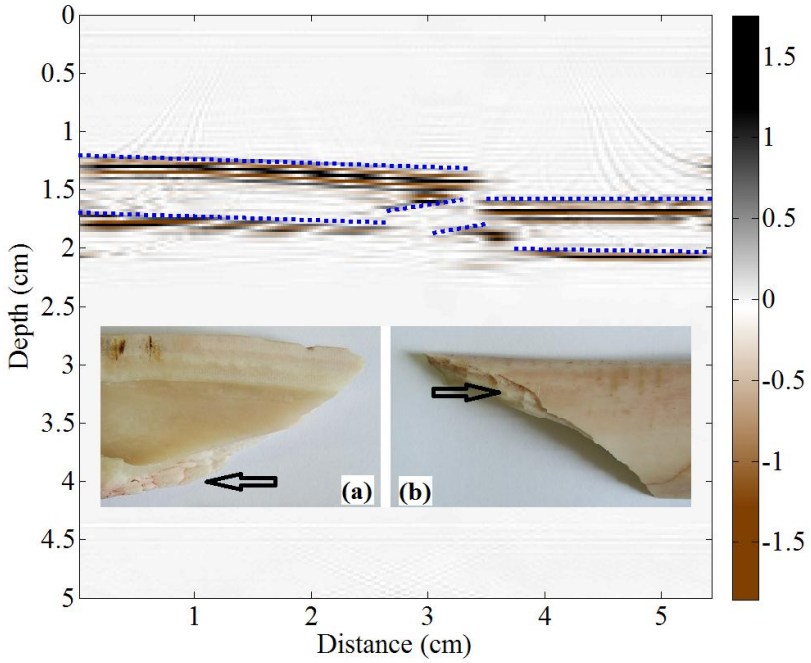

Figure 4.13: The reconstructed image of the fractured bone plate. The subfigures point out the corresponding fracture parts: (a) the flipped left part of the fracture and (b) the right part of the fracture.

For the irregular shaped bone plate and fracture, all the reflected signals change significantly compared to the regular shaped phantom. In addition, the attenuation in the bone plate is so large that the reflected signals decrease quickly. However, the reconstructed depth-offset image can still provide us better information about the geometry of the bone plate and the fracture, such as the thickness, position, and shape, which is more accurate than the information provided by the original time-distance echograms.

4.4 Image reconstruction of the fractured bone

Another measurement is conducted on a cracked bovine long bone, with marrow in the middle cavity as shown in Figure 4.14. The blue line outlines the track along which the transducer moves. We can see that the fracture size is small around 1-2 mm.

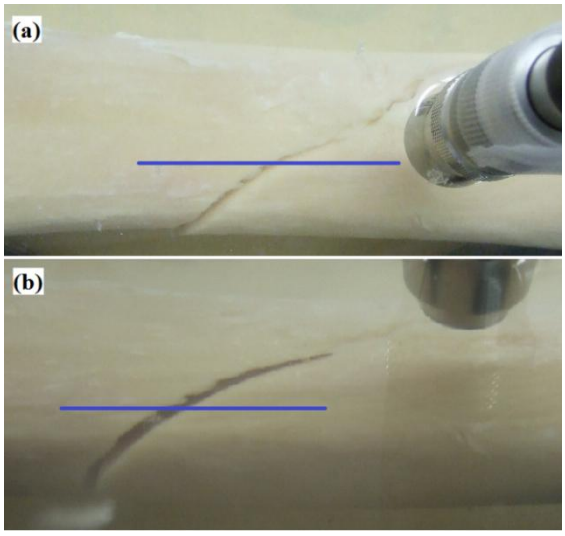

Figure 4.14: Image of the cracked bovine long bone: (a) top view and (b) side view.

The recorded echogram is shown in Figure 4.15. As we discussed earlier, only one cortical bone layer can be detected in the reflected signals. Due to the energy absorption and scattering, reflected signals from the lower cortical bone are too small to be seen. Because the bovine cortical bone is thicker (around 7 mm) than the deer bone (around 5 mm), the echoes from the lower surface of the cortex become smaller in amplitude than those of the bone plate. From the image, we circle the areas where there is a break in the recorded signals. We suspect those areas are the fracture locations.

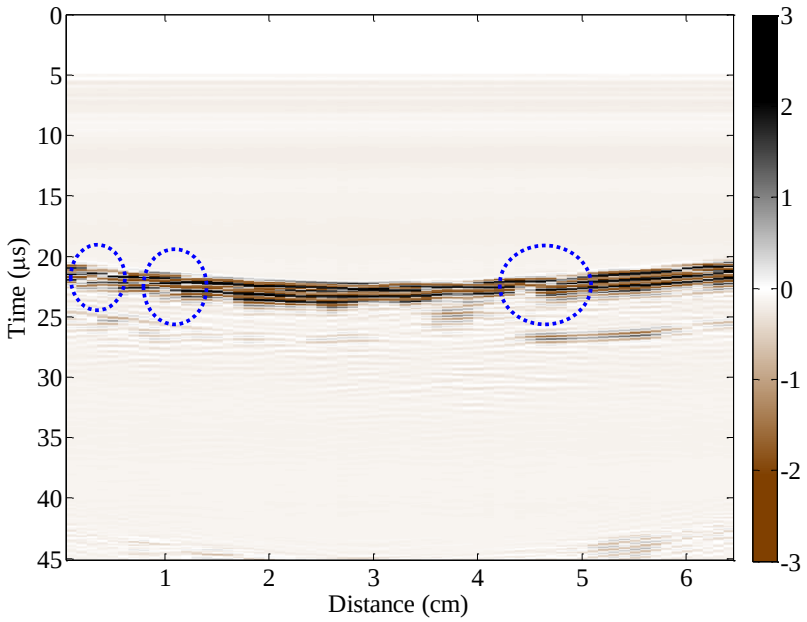

Figure 4.15: The recorded echogram for the cracked bovine long bone. Blue circles highlight the suspected fractured areas.

The recorded signals are processed before migration. After gain, interpolation and normalization, the signals are enhanced, as shown in Figure 4.16. Compared

with Figure 4.15, a big improvement is achieved for the weak reflected signals, especially the reflections between the upper and lower interfaces of the cortical bone. For the lower cortical bone surface reflections, there is a gap in the signals between 3.2 and 4.5 cm, which also indicates that a fracture locates just above this area. So after the signal processing, the position of the fracture can be estimated. Migration will give us more accurate information where the fracture locates, including both depth and distance.

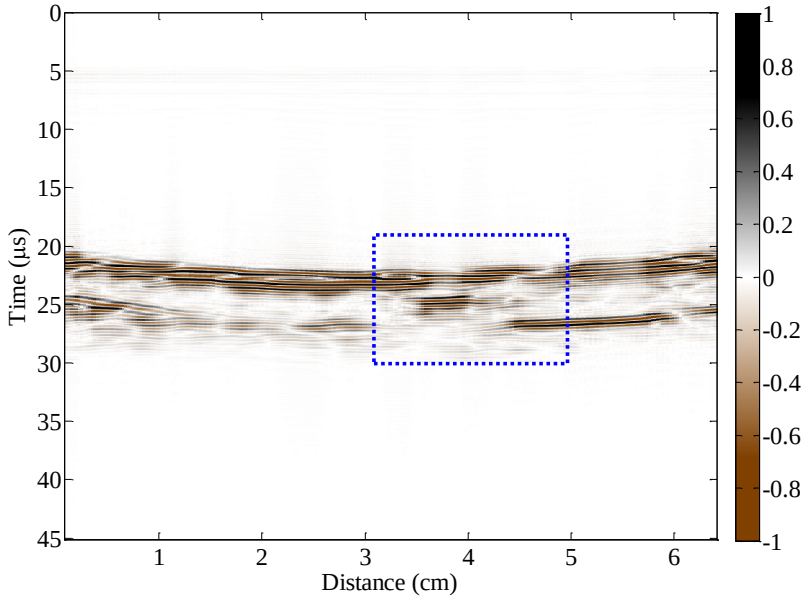

Figure 4.16: The processed echogram, with the enhancement of the weak reflections. Blue rectangle outlines the fracture area.

For the migration process, a velocity model is first constructed, as shown in Figure 4.17. Ultrasound velocity in cortical bone is set to be 3600 m/s and the velocity of water and marrow is 1500 m/s. The interfaces between different velocities are smoothed, making the transition area around 5 mm thick to

eliminate the computational error. The velocity model is used directly in the migration process.

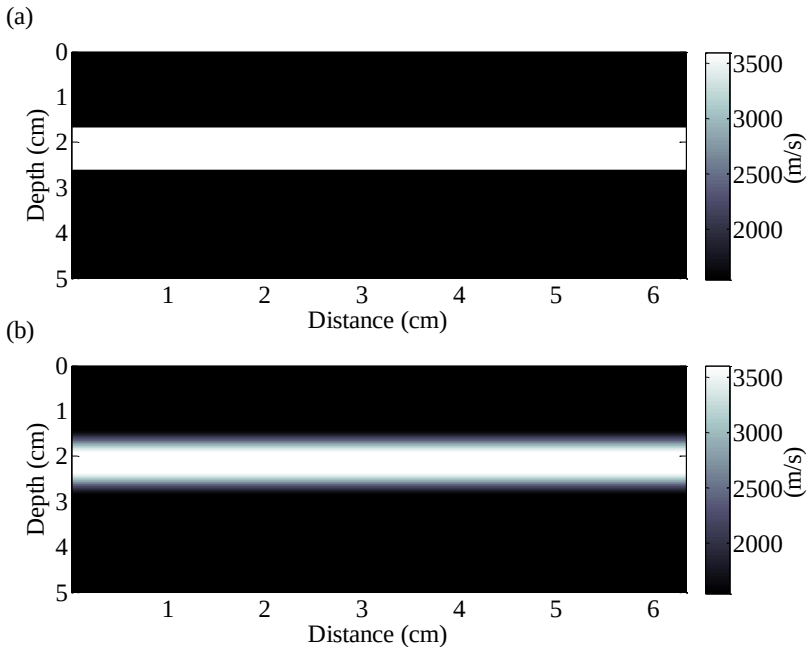

Figure 4.17: Velocity model for the reconstruction of the bovine long bone image: (a) the original velocity model and (b) a smoothed version of (a).

Using the SSFM method, we migrate the data and the reconstructed image is shown in Figure 4.18. Blue dots contour the interfaces from the reconstructed image. From the image, we obtain the thickness of the cortical bone, which is about 6-7 mm. The shape of the fracture part is also obtained in the image. Due to the small size and the irregular shape of the fracture, it is difficult to get an exact contour of the fracture. However, the blue dotted curve still provides a rough idea about the fracture shape. Compared with the real fracture shape in the subfigure, the reconstructed image yields a fairly accurate result. We notice that as the

cortical bone thickness becomes larger, the reflected signals from the top surface of bone have many cycles, lose resolution, causing the reconstructed surface thicker. This is due to the inhomogeneity of the cortical bone. However, this effect will not affect our imaging results, as long as the interface is well imaged.

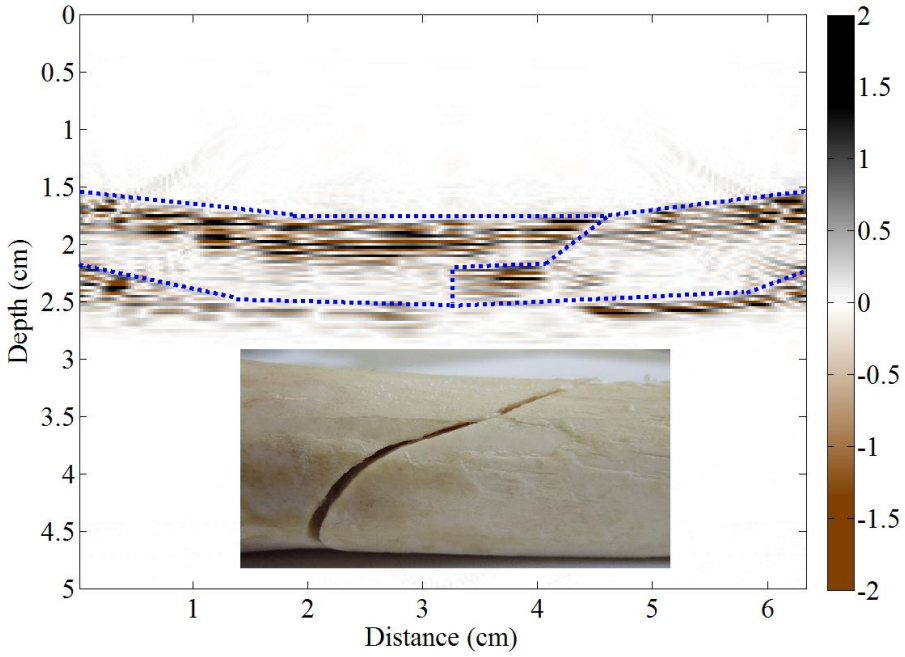

Figure 4.18: The reconstructed image for the top cortex of the bovine long bone. The blue dotted curve outlines the fracture. The subfigure presents a side view image of the fracture.

4.5 Summary

In this chapter, we described the experiment setup and discussed the experiment on a Plexiglas phantom, a deer bone plate, and a bovine long bone. All the received data are processed before migration. The processing steps include band-pass filter, time gain compensation, interpolation and normalization. The SSFM

method was used to reconstruct the fracture images. From the image, we attempted to retrieve the information such as the sample thickness, fracture shapes, and dimensions.

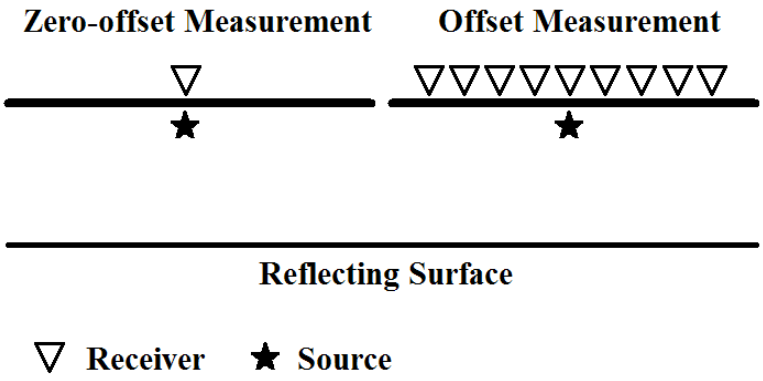

Figure 4.19: A schematic of the zero-offset and offset measurement.

The results have demonstrated a possibility of using ultrasound to image real bone. However experiment results can be further improved in a future study. First, the acquired signals are quite weak. It is partly due to the zero-offset measurement, where the source and receiver are at the same location and the beam is not normal to the fracture surface. If the offset case is used as shown in Figure 4.19, more receivers will be used to receive echoes at an oblique angle from the fracture interface. The signal quality and strength can be improved. Also, the transducer element size is too big in the experiment (6 mm), which will definitely lower the resolution of the signals due to averaging. Besides, the acquisition spacing interval of one millimeter per record is too large to get a good resolution image. So to improve the data quality in the experiment, we must reduce transducer

element size, try an offset measurement configuration, and also reduce spacing intervals.

Chapter 5. Conclusions

Ultrasound techniques have been widely used in many fields. Ultrasound imaging is becoming an increasingly important diagnostic method in medical fields. Compared with other diagnostic imaging methods, such as X-ray, CT and MRI, ultrasound is less expensive so that it is affordable in even less developed regions. Also, ultrasound has no ionizing radiation, making it a preferable tool in diagnostics on infants and children. Besides, ultrasound diagnostic equipment is small and portable, and thus is suitable for emergency use. Over the years with the pulse-echo technique and the Doppler technique, ultrasound has played an important role in diagnostic imaging, especially on soft tissue, vessels and blood.

In this thesis, we examined the possibility of using ultrasound to image long bone structure, such as cortical bone thickness and shape of bone fractures. The seismic migration method, a method mainly applied in Geophysics to image subsurface structures, was introduced in our study. Numerical experiments using both zero-offset reverse time migration (RTM) and split step Fourier migration (SSFM) were performed. The results were used to assess the possibility of utilizing migration to reconstruct bone internal structures, both intact and fractured, test the robustness of the method, and explore the limitations of the method. Experiments were also carried out on phantoms and real bones to illustrate the migrated results on real data.

From the studies using numerical and experimental data, several conclusions can be drawn as follows.

Wave-equation based migration technique is a promising tool that can be used to image long bones. The numerical experiments discussed in this thesis have provided us with some justification of the methodology. Although some information can be derived directly from the recorded time signals such as the existence of an anomaly (the scatterers which cause the reflected signals), or the proximal offset position of the anomaly, we cannot obtain depth information or the exact position of the reflectors. The imaging method discussed in this thesis is able to refocus the reflected energy back to the originating points, providing the structural information of the reflectors. From the migrated image, we can tell where the reflections originate from and depict the internal structures. The thickness of the cortical bone can be obtained directly from the migrated image. The shapes and dimensions of the fractures can be estimated. Experimental data pose some challenges as the data is not as well presented as the numerical simulations due to the transducer condition as well as the complexity in real bone. However, the migrated images have provided us with more detailed and direct information about the sample structure.

Two different migration methods were examined. For the choice of reverse time migration and split step Fourier migration, the RTM has a better migrated result than the SSFM. However, the RTM method is much more time consuming

than the SSFM method and thus is not suitable for real time application in clinical cases unless a fast computing method such as parallel computing is used. The drawback of the SSFM method comes from the approximation of velocity in its algorithm. This can be eliminated through an iterative migration method, in which the migrated image of the first pass is used to reconstruct a new velocity model for the second pass. Several iterations may be necessary before achieving a desirable result.

The zero-offset data acquisition configuration is simple and has provided comparatively good results using numerical simulation and experimental data. However, the zero-offset configuration cannot handle vertical interfaces due to the lack of reflection signals. An offset data acquisition configuration, which has one transmitting transducer and multiple receivers located at different offsets, is more suitable as the offset transducers will receive the obliquely reflected energy from the material defects. Active element size and measurement spacing interval should be as small as possible in order to achieve better resolution.

To summarize, we have presented a possible way of applying seismic migration methods to image long bone structures, including cortical bone thickness, bone fracture and fracture healing. Through numerical modeling on various idealized models and experiments on phantom and real bones, we have demonstrated that wave equation based migration is a promising way to image long bones and the reconstructed images can provide us with more direct and

accurate information of the sample's internal structure than the traditional ultrasound reflection time-distance echograms.

Bibliography

Ackermann, O., Liedgens, P., Eckert, K., Chelangattucherry, E., Husain, B., and Ruchholtz, S. (**2009**). "Ultrasound diagnosis of forearm fractures in children. A prospective multicenter study," Unfallchirurg **112**, 706-711.

Albertin, U., Watts, D., Chang, W., Kapoor, S. J., Stork, C., Kitchenside, P., and Yingst, D. (**2002**). "Near-salt-flank imaging with Kirchhoff and wavefield-extrapolation migration," SEG Technical Program Expanded Abstracts **21**, 1328-1331.

Atkinson, P., and Lennon, R. (**2003**). "Use of emergency department ultrasound in the diagnosis and early management of femoral fractures," Emergency Medicine Journal **20**, 395-395.

Augat, P., Merk, J., Genant, H. K., and Claes, L. (**1997**). "Quantitative Assessment of Experimental Fracture Repair by Peripheral Computed Tomography," Calcified Tissue International **60**, 194-199.

Bavu, E., Besnainou, C., Gibiat, V., de Rosny, J., and Fink, M. (**2007**). "Subwavelength sound focusing using a time-reversal acoustic sink," Acta Acustica United with Acustica **93**, 706-715.

Baysal, E., Kosloff, D. D., and Sherwood, J. W. C. (**1983**). "Reverse time migration," Geophysics **48**, 1514-1524.

Beylkin, G. (**1985**). "Imaging of discontinuities in the inverse scattering problem by inversion of a causal generalized Radon transform," Journal of Mathematical Physics **26**, 99-108.

Blokhuis, T. J., den Boer, F. C., Bramer, J. A. M., van Lingen, A., Roos, J. C., Bakker, F. C., Patka, P., and Haarman, H. J. T. M. (**2000**). "Evaluation of Strength of Healing Fractures With Dual Energy Xray Absorptiometry," Clinical Orthopaedics and Related Research **380**, 260-268.

Bording, R. P., and Lines, L. R. (**1997**). *Seismic modeling and imaging with the complete wave equation* (Society of Exploration Geophysicists).

Burge, R., Dawson-Hughes, B., Solomon, D. H., Wong, J. B., King, A., and Tosteson, A. (**2007**). "Incidence and Economic Burden of Osteoporosis-Related Fractures in the United States, 2005–2025," Journal of Bone and Mineral Research **22**, 465-475.

Cattermole, H. C., Fordham, J. N., Muckle, D. S., and Cunningham, J. L. (**1996**). "Dual-Energy X-Ray Absorptiometry as a Measure of Healing in Fractures Treated by Intramedullary Nailing," Journal of Orthopaedic Trauma **10**, 563-568.

Chang, Y.-F., Wang, C.-Y., and Hsieh, C.-H. (**2001**). "Feasibility of detecting embedded cracks in concrete structures by reflection seismology," NDT & E International **34**, 39-48.

Chang, Y. F., and Chern, C. C. (**2000**). "Frequency-wavenumber migration of ultrasonic data," Journal of Nondestructive Evaluation **19**, 1-10.

Chang, Y. F., and Ton, R. C. (**2001**). "Kirchhoff migration of ultrasonic images," Mater. Eval. **59**, 413-417.

Chun, H. W. (**2004**). "A synthetic time-reversal imaging method for structural health monitoring," Smart Materials and Structures **13**, 415.

Claerbout, J. F. (**1971**). "Toward a unified theory of reflector mapping," Geophysics **36**, 467-481.

Claerbout, J. F. (**1985**). *Imaging the earth's interior* (Blackwell Scientific Publications, Inc.).

Claire, P. (**2002**). "Time reversal techniques in ultrasonic nondestructive testing of scattering media," Inverse Problems **18**, 1761.

Craig, J. G., Jacobson, J. A., and Moed, B. R. (**1999**). "Ultrasound of fracture and bone healing," Radiologic Clinics of North America **37**, 737-751.

Derode, A., Roux, P., and Fink, M. (**1995**). "Robust acoustic time reversal with high-order multiple scattering," Physical Review Letters **75**, 4206.

Dimitriou, R., Tsiridis, E., and Giannoudis, P. V. (**2005**). "Current concepts of molecular aspects of bone healing," Injury **36**, 1392-1404.

Doblar, M., Garcia, J. M., and Gomez, M. J. (**2004**). "Modelling bone tissue fracture and healing: a review," Engineering Fracture Mechanics **71**, 1809-1840.

Dodd, S. P., Cunningham, J. L., Miles, A. W., Gheduzzi, S., and Humphrey, V. F. (**2007a**). "An in vitro study of ultrasound signal loss across simple

fractures in cortical bone mimics and bovine cortical bone samples," Bone **40**, 656-661.

Dodd, S. P., Cunningham, J. L., Miles, A. W., Gheduzzi, S., and Humphrey, V. F. (**2008**). "Ultrasound Transmission Loss Across Transverse and Oblique Bone Fractures: An In Vitro Study," Ultrasound in Medicine & Biology **34**, 454-462.

Dodd, S. P., Miles, A. W., Gheduzzi, S., Humphrey, V. F., and Cunningham, J. L. (**2007b**). "Modelling the effects of different fracture geometries and healing stages on ultrasound signal loss across a long bone fracture," in *Computer Methods in Biomechanics & Biomedical Engineering* (Taylor & Francis Ltd), pp. 371-375.

Edelmann, G. F., Song, H. C., Kim, S., Hodgkiss, W. S., Kuperman, W. A., and Akal, T. (**2005**). "Underwater acoustic communications using time reversal," Oceanic Engineering, IEEE Journal of **30**, 852-864.

Fardellone, P. (**2008**). "Predicting the fracture risk in 2008," Joint Bone Spine **75**, 661-664.

Fehler, M. C., and Huang, L. (**2002**). "Modern imaging using seismic reflection data," Annual Review of Earth and Planetary Sciences **30**, 259-284.

Fink, M. (**1992**). "Time reversal of ultrasonic fields-part I: basic principles," Ieee Transactions on Ultrasonics Ferroelectrics and Frequency Control **39**, 555-566.

Fink, M. (**2006**). "Time-reversal acoustics in complex environments," Geophysics **71**, SI151-SI164.

Fink, M., de Rosny, J., Lerosey, G., and Tourin, A. (**2009**). "Time-reversed waves and super-resolution," Comptes Rendus Physique **10**, 447-463.

Fink, M., Montaldo, G., and Tanter, M. (**2003**). "Time-reversal acoustics in biomedical engineering," Annual Review of Biomedical Engineering **5**, 465-497.

Fink, M., Prada, C., Wu, F., and Cassereau, D. (**1989**). "Self focusing in inhomogeneous media with time reversal acoustic mirrors," in *Ultrasonics Symposium, 1989. Proceedings., IEEE 1989*, pp. 681-686 vol.682.

Finkelstein, E. A., Corso, P. S., and Miller, T. R. (**2006**). *Incidence and economic burden of injuries in the United States* (Oxford University Press).

Gazdag, J. (**1978**). "Wave equation migration with the phase-shift method," Geophysics **43**, 1342-1351.

Gazdag, J., and Sguazzero, P. (**1984a**). "Migration of seismic data," Proceedings of the IEEE **72**, 1302-1315.

Gazdag, J., and Sguazzero, P. (**1984b**). "Migration of seismic data by phase shift plus interpolation," Geophysics **49**, 124-131.

Gheduzzi, S., Dodd, S. P., Miles, A. W., Humphrey, V. F., and Cunningham, J. L. (**2009**). "Numerical and experimental simulation of the effect of long bone fracture healing stages on ultrasound transmission across an idealized fracture," Journal of the Acoustical Society of America **126**, 887-894.

Gray, S. H., Etgen, J., Dellinger, J., and Whitmore, D. (**2001**). "Seismic migration problems and solutions," Geophysics **66**, 1622-1640.

Gupta, H. S., and Zioupos, P. (**2008**). "Fracture of bone tissue: The 'hows' and the 'whys'," Medical Engineering & Physics **30**, 1209-1226.

Heinemann, M., Larraza, A., and Smith, K. B. (**2003**). "Experimental studies of applications of time-reversal acoustics to noncoherent underwater communications," The Journal of the Acoustical Society of America **113**, 3111-3116.

Heiner, J. D., and McArthur, T. J. (**2009**). "A Simulation Model for the Ultrasound Diagnosis of Long-Bone Fractures," Simul. Healthc. **4**, 228-231.

Huang, L.-J., Fehler, M. C., and Wu, R.-S. (**1999**). "Extended local Born Fourier migration method," Geophysics **64**, 1524-1534.

Huang, L., Duric, N., and Littrup, P. (**2006**). "Breast imaging with time-reversed ultrasound," edited by E. Stanislav, and F. W. William (SPIE), p. 61470I.

Huang, L., Duric, N., and Littrup, P. J. (**2003**). "Ultrasonic breast imaging using a wave-equation migration method," edited by F. W. William, and F. I. Michael (SPIE), pp. 432-439.

Huang, L., and Quan, Y. (**2007**). "Ultrasound pulse-echo imaging using the split-step Fourier propagator," in *Medical Imaging 2007: Ultrasonic Imaging and Signal Processing* (SPIE, San Diego, CA, USA), pp. 651305-651312.

Huang, L. J., Hanson, K. M., Quan, Y. L., Li, C. P., and Duric, N. (**2008**). "Globally optimized Fourier finite-difference method for ultrasound breast imaging - art. no. 692007," Medical Imaging 2008: Ultrasonic Imaging and Signal Processing **6920**, 92007-92007.

Hubner, U., Schlicht, W., Outzen, S., Barthel, M., and Halsband, H. (**2000**). "Ultrasound in the diagnosis of fractures in children," J Bone Joint Surg Br **82-B**, 1170-1173.

Laugier, P., and Haiat, G. (eds). (**2011**). *Bone Quantitative Ultrasound* (Springer Netherlands).

Le, L. H., Gu, Y. J., Li, Y., and Zhang, C. (**2010**). "Probing long bones with ultrasonic body waves," Applied Physics Letters **96**, 114102-114103.

Legome, E., and Pancu, D. (**2004**). "Future applications for emergency ultrasound," Emergency Medicine Clinics of North America **22**, 817-827.

Liu, Q. H. (**1997**). "The PSTD algorithm: A time-domain method requiring only two cells per wavelength," (Wiley Subscription Services, Inc., A Wiley Company), pp. 158-165.

Loewenthal, D., Lu, L., Roberson, R., and Sherwood, J. (**1976**). "The wave equation applied to migration," Geophysical Prospecting **24**, 380-399.

Lowet, G., and Van der Perre, G. (**1996**). "Ultrasound velocity measurement in long bones: Measurement method and simulation of ultrasound wave propagation," Journal of Biomechanics **29**, 1255-1262.

Maffulli, N., and Thornton, A. (**1995**). "Ultrasonographic appearance of external callus in long-bone fractures," Injury **26**, 5-12.

Martini, F. H., Timmons, M. J., Tallitsch, R. B., Ober, W. C., Garrison, C. W., Welch, K., and Hutchings, R. T. (**2005**). *Human Anatomy* (Benjamin Cummings).

Matsuyama, J., Ohnishi, I., Sakai, R., Bessho, M., Matsumoto, T., Miyasaka, K., Harada, A., Ohashi, S., and Nakamura, K. (**2008**). "A New Method for Evaluation of Fracture Healing by Echo Tracking," Ultrasound in Medicine & Biology **34**, 775-783.

McManus, J. G., Morton, M. J., Crystal, C. S., McArthur, T. J., Helphenstine, J. S., Masneri, D. A., Young, S. E., and Miller, M. A. (**2008**). "Use of ultrasound to assess acute fracture reduction in emergency care settings," Am J Disaster Med **3**, 241-247.

McMechan, G. A. (**1983**). "Migration by extrapolation of time-dependent boundary values," Geophysical Prospecting **31**, 413-420.

Miller, D., Oristaglio, M., and Beylkin, G. (**1987**). "A new slant on seismic imaging; migration and integral geometry," Geophysics **52**, 943-964.

Moed, B. R., Subramanian, S., van Holsbeeck, M., Watson, J. T., Cramer, K. E., Karges, D. E., Craig, J. G., and Bouffard, J. A. (**1998**). "Ultrasound for the early diagnosis of tibial fracture healing after static interlocked nailing without reaming: Clinical results," Journal of Orthopaedic Trauma **12**, 206-213.

Moorcroft, C. I., Ogrodnik, P. J., Thomas, P. B. M., and Wade, R. H. (**2001**). "Mechanical properties of callus in human tibial fractures: a preliminary investigation," Clinical Biomechanics **16**, 776-782.

Moritz, J. D., Berthold, L. D., Soenksen, S. F., and Alzen, G. F. (**2008**). "Ultrasound in diagnosis of fractures in children: Unnecessary harassment or useful addition to X-ray?," Ultraschall Med. **29**, 267-274.

Morshed, S., Corrales, L., Genant, H., and Miclau, T., III (**2008**). "Outcome Assessment in Clinical Trials of Fracture-Healing," J Bone Joint Surg Am **90**, 62-67.

Mufti, I. R., Pita, J. A., and Huntley, R. W. (**1996**). "Finite-difference depth migration of exploration-scale 3-D seismic data," Geophysics **61**, 776-794.

Mulder, W. A., and Plessix, R.-E. (**2004**). "A comparison between one-way and two-way wave-equation migration," Geophysics **69**, 1491-1504.

Nakatsuchi, Y., Tsuchikane, A., and Nomura, A. (**1996**). "Assessment of Fracture Healing in the Tibia Using the Impulse Response Method," Journal of Orthopaedic Trauma **10**, 50-62.

Operto, M. S., Xu, S., and Lambare, G. (**2000**). "Can we quantitatively image complex structures with rays?," Geophysics **65**, 1223-1238.

Phillips, A. M. (**2005**). "Overview of the fracture healing cascade," Injury **36**, S5-S7.

Prosser, W. H., Seale, M. D., and Smith, B. T. (**1999**). "Time-frequency analysis of the dispersion of Lamb modes," The Journal of the Acoustical Society of America **105**, 2669-2676.

Protopappas, V. C., Fotiadis, D. I., and Malizos, K. N. (**2006**). "Guided ultrasound wave propagation in intact and healing long bones," Ultrasound in Medicine and Biology **32**, 693-708.

Protopappas, V. C., Kourtis, I. C., Kourtis, L. C., Malizos, K. N., Massalas, C. V., and Fotiadis, D. I. (**2007**). "Three-dimensional finite element modeling of guided ultrasound wave propagation in intact and healing long bones," The Journal of the Acoustical Society of America **121**, 3907-3921.

Protopappas, V. C., Vavva, M. G., Fotiadis, D. I., and Malizos, K. N. (**2008**). "Ultrasonic monitoring of bone fracture healing," Ultrasonics, Ferroelectrics and Frequency Control, IEEE Transactions on **55**, 1243-1255.

Ristow, D., and Ruhl, T. (**1994**). "Fourier finite-difference migration," Geophysics **59**, 1882-1893.

Santos, L. T., Schleicher, J., Tygel, M., and Hubral, P. (**2000**). "Seismic modeling by demigration," Geophysics **65**, 1281-1289.

Schindeler, A., McDonald, M. M., Bokko, P., and Little, D. G. (**2008**). "Bone remodeling during fracture repair: The cellular picture," Seminars in Cell & Developmental Biology **19**, 459-466.

Schneider, W. A. (**1978**). "Integral formulation for migration in two and three dimensions," Geophysics **43**, 49-76.

Spitz, S. (**1991**). "Seismic trace interpolation in the F-X domain," Geophysics **56**, 785-794.

Stoffa, P. L., Fokkema, J. T., Freire, R. M. d. L., and Kessinger, W. P. (**1990**). "Split-step Fourier migration," Geophysics **55**, 410-421.

Strikwerda, J. C. (**1989**). *Finite difference schemes and partial differential equations* (Wadsworth Publ. Co.).

Tarantola, A. (**1984**). "Inversion of seismic reflection data in the acoustic approximation," Geophysics **49**, 1259-1266.

Taylor, J. R. (**1972**). *Scattering Theory* (John Wiley and Sons, Inc).

Wapenar, C. P. A., and Berkhout, A. (**1989**). *Elastic wavefield extrapolation* (Elsevier Science Publishing Company Inc.).

Weinberg, E. R., Tunik, M. G., and Tsung, J. W. (**2010**). "Accuracy of clinician-performed point-of-care ultrasound for the diagnosis of fractures in children and young adults," Injury-Int. J. Care Inj. **41**, 862-868.

Wells, P. N. T. (**1983**). "Ultrasonic imaging," in *Scientific basis of medical imaging*, edited by P. N. T. Wells, pp. 138-193.

Whitmore, N. D. (**1984**). "Iterative depth migration by backward time propagation," Geophysics **49**, 640-640.

Wu, F., Thomas, J. L., and Fink, M. (**1992**). "Time reversal of ultrasonic fields-part II: experimental results," Ieee Transactions on Ultrasonics Ferroelectrics and Frequency Control **39**, 567-578.